

# Field-aligned and ionospheric currents by AMPERE and SuperMAG during HSS/SIR-driven storms

M. N. Pedersen<sup>1</sup>, H. Vanhamäki<sup>1</sup>, A. T. Aikio<sup>1</sup>, S. Käki<sup>2,3</sup>, A. B. Workayehu<sup>1</sup>,  
C. L. Waters<sup>4</sup>, J. W. Gjerloev<sup>5,6</sup>

<sup>1</sup>Space physics and Astronomy Research Unit, University of Oulu, Oulu, Finland

<sup>2</sup>Finnish Meteorological Institute, Helsinki, Finland

<sup>3</sup>Division of Particle Physics and Astrophysics, University of Helsinki, Helsinki, Finland

<sup>4</sup>School of Mathematical and Physical Sciences, University of Newcastle, Callaghan, New South Wales,  
Australia

<sup>5</sup>The Johns Hopkins University Applied Physics Laboratory, Laurel, MD, USA

<sup>6</sup>Faculty for physics and technology, University of Bergen, Bergen, Norway

## Key Points:

- The integrated FAC and equivalent currents peak 40 and 58 min after storm onset, respectively.
- The currents are strongly driven by the solar wind as indicated by the  $\varepsilon$  parameter and the correlation coefficient between  $\varepsilon$  and FAC is 0.90.
- High  $p_{\text{dyn}}$  storms produce SSCs, larger SW coupling, the first peak in auroral currents, and a longer recovery phase than low  $p_{\text{dyn}}$  storms.

---

Corresponding author: Pedersen, M. N., [marcus.pedersen@oulu.fi](mailto:marcus.pedersen@oulu.fi)

## Abstract

This study considers 28 geomagnetic storms with  $Dst \leq -50$  nT driven by high-speed streams (HSSs) and associated stream interaction regions (SIRs) during 2010-2017. Their impact on ionospheric horizontal and field-aligned currents (FACs) have been investigated using superposed epoch analysis of SuperMAG and AMPERE data, respectively. The zero epoch ( $t_0$ ) was set to the onset of the storm main phase. Storms begin in the SIR with enhanced solar wind density and compressed southward oriented magnetic field. The integrated FAC and equivalent currents maximise 40 and 58 min after  $t_0$ , respectively, followed by a small peak in the middle of the main phase ( $t_0+4h$ ), and a slightly larger peak just before the  $Dst$  minimum ( $t_0+5.3h$ ). The currents are strongly driven by the solar wind, and the correlation between the Akasofu  $\varepsilon$  and integrated FAC is 0.90. The number of substorm onsets maximises near  $t_0$ . The storms were also separated into two groups based on the solar wind dynamic pressure  $p_{dyn}$  in the vicinity of the SIR. High  $p_{dyn}$  storms reach solar wind velocity maxima earlier and have shorter lead times from the HSS arrival to storm onset compared with low  $p_{dyn}$  events. The high  $p_{dyn}$  events also have sudden storm commencements, stronger solar wind driving and ionospheric response at  $t_0$ , and are primarily responsible for the first peak in the currents after  $t_0$ . After  $t_0 + 2$  days, the currents and number of substorm onsets become higher for low compared with high  $p_{dyn}$  events, which may be related to higher solar wind speed.

## Plain Language Summary

Solar wind emanating from solar coronal holes tend to have faster velocity than the ambient solar wind and can together with southward oriented interplanetary magnetic field lead to geomagnetic storms in geospace. We have studied 28 geomagnetic storms of this kind and analysed the behaviour of the field-aligned currents and ionospheric horizontal currents in the high latitude auroral region with respect to the onset of the geomagnetic storms. The total current maximizes just 40 minutes after the storm onset, followed by two smaller peaks in the middle and end of the storm main phase. The correlation between the total field-aligned current and the predicted solar wind-magnetosphere coupling is very high, 0.90, and indicates that the currents are strongly driven by the solar wind. We also split the storms into two groups based on the solar wind dynamic pressure at the onset of the storms. Several characteristic differences are found between the two groups, e.g. high pressure storms are largely responsible for the first peak in the currents and have shorter lead time between the coronal hole solar wind is detected by upstream satellites and the onset of the storm. These findings could help improve space weather predictions.

## 1 Introduction

Gonzalez et al. (1994) defined a geomagnetic storm as an interval of time when a sufficiently intense and long-lasting interplanetary convection electric field leads, through a substantial energization in the magnetosphere-ionosphere system, to an intensified ring current strong enough to exceed some key threshold of the quantifying storm time  $Dst$  index. The two processes responsible for causing the majority of storms are interplanetary coronal mass ejections (ICMEs) and high speed streams (HSSs) with their associated solar wind stream interaction regions (SIRs) (Kamide, Baumjohann, et al., 1998a,b).

HSS is solar wind emanating from coronal holes on the Sun with substantially higher velocity than the ambient solar wind (SW) (Krieger et al., 1973; Neupert & Pizzo, 1974). At the interface between the slow and fast SW, a region of compressed density and interplanetary magnetic field (IMF) develops that is often accompanied by a change in direction of the SW flow velocity (Gosling et al., 1978). These regions are known as SIRs, or co-rotating interaction regions (CIRs) if the coronal hole persists for more than one solar rotation (Balogh et al., 1999; Jian et al., 2006). Some papers (e.g. Jian et al., 2006) use the term SIR for

68 interaction regions that are only seen during one solar rotation, as opposed to the longer  
 69 lasting CIR, but in this article we use the term SIR for any stream interaction region, re-  
 70 gardless of the duration. HSS/SIRs occur most frequently during the declining phases of  
 71 solar cycles (Gonzalez et al., 1999; Tsurutani et al., 2006; Grandin et al., 2019) and are  
 72 the most frequent sources of weak-to-moderate ( $Dst > -100$  nT) storms (Zhang et al., 2008;  
 73 Richardson & Cane, 2012). In contrast, ICMEs are the most common source of large and  
 74 major ( $Dst < -100$  nT) storms and are most frequently observed during solar cycle maxima  
 75 (Webb & Howard, 1994; Borovsky & Denton, 2006).

76 Although ICMEs give rise to the strongest storms, HSS/SIRs typically are of longer du-  
 77 ration and have longer lasting impact on the Earth’s magnetosphere-ionosphere-thermosphere  
 78 (MIT) system (Turner et al., 2009; Burns et al., 2012). The presence of Alfvénic fluctua-  
 79 tions have been observed in the SW of HSS/SIRs. This Alfvénic activity consists of large-  
 80 amplitude quasi-periodic fluctuations in the orientation of the IMF with periods ranging  
 81 from tens of minutes to a few hours (Belcher & Davis Jr, 1971; Kamide, Baumjohann,  
 82 et al., 1998b; Tanskanen et al., 2017). Alfvénic activity in HSS/SIR storms can prolong  
 83 the storm recovery phase by allowing for frequent and recurring reconnection between the  
 84 SW and magnetosphere that in turn drives substorms. This type of substorms and iono-  
 85 spheric current activity is known as high intensity, long duration continuous auroral activity  
 86 (HILDCAA) events (Tsurutani & Gonzalez, 1987). An additional factor that may affect the  
 87 occurrence and duration of storms is the Russell-McPherron effect (Russell & McPherron,  
 88 1973; Zhao & Zong, 2012; Lockwood et al., 2020). Russell & McPherron (1973) showed  
 89 the varying probability of southward IMF orientation throughout the year as seen by the  
 90 Earth’s magnetosphere that maximizes at the equinoxes. This is caused by the varying angle  
 91 between the Y axis in the solar equatorial coordinate system (where the IMF is ordered),  
 92 and the Z axis of the solar magnetospheric coordinate system (where the coupling between  
 93 the SW/IMF and magnetosphere is ordered).

94 A magnetic storm usually contains many individual magnetospheric substorms. During  
 95 substorms, both horizontal currents and Birkeland currents, also known as field-aligned cur-  
 96 rents or FACs, intensify. Several studies have focused on the connection between substorms  
 97 and the ionospheric currents (e.g. Coxon et al., 2014a; McPherron et al., 2018). Coxon et  
 98 al. (2014b) reported results from a superposed epoch analysis (SEA) study of substorms,  
 99 where they analysed the magnitude and spatial evolution of the Region 1 (R1) and Region  
 100 2 (R2) FACs and found that each current system increased in magnitude by up to 1.25 MA  
 101 over the course of a substorm cycle.

102 The statistical patterns of Birkeland currents have been studied in several papers, and  
 103 they are typically presented as a function of the IMF direction and magnitude, although  
 104 other parameters may be used (Iijima & Potemra, 1978; Weimer, 2001; Anderson et al.,  
 105 2008; Juusola et al., 2009; Laundal et al., 2018; Workayehu et al., 2020). Anderson et al.  
 106 (2005) stated that “While statistical patterns of Birkeland currents are well known, we know  
 107 little about their storm-time characteristics, in part because storm-time current systems do  
 108 not repeat in the same sequence from storm to storm”. The main aim of our study is to  
 109 address this question for HSS/SIR-driven storms. In addition to the FACs, we also study  
 110 the evolution of the horizontal equivalent currents in the ionosphere during the HSS/SIR  
 111 storms.

112 Numerous studies have considered the impact of IMF, the solar wind electric field  $E_Y$   
 113 or some other coupling function depending on IMF direction, magnitude and solar wind  
 114 velocity on the magnetosphere and ionosphere, as these are the main parameters governing  
 115 solar wind-magnetospheric coupling (see e.g. Dungey, 1961; Rostoker & Fälthammar, 1967;  
 116 Akasofu, 1981, and references therein). Korth et al. (2010) studied the effect that different  
 117 SW and IMF parameters have on the intensity of the FACs and found that the impact of  
 118 SW dynamic pressure was modest compared to  $E_Y$ . It has been found that the dynamic  
 119 pressure has the most prominent impact on the magnetosphere-ionosphere-thermosphere  
 120 system under steady  $B_Z$  negative orientation (e.g. Boudouridis et al., 2003, 2004, 2005).

121 Solar wind dynamic pressure has been omitted in many solar wind-magnetosphere energy  
 122 coupling functions, as it had long been thought to not play a major role in the energy transfer  
 123 (Akasofu, 1981), but later studies (e.g. Newell et al., 2008) have shown that including the  
 124 dynamic pressure can make significant improvements in the predictions.

125 The global distribution and response of FACs and equivalent horizontal currents with  
 126 high time resolution (10 min) to HSS/SIR driven storms has not been studied earlier. The  
 127 aim of this study is to examine the effect of HSS/SIR driven storms have on the temporal and  
 128 spatial evolution of FACs and ionospheric currents on time scale of storms ( $\sim$  days) using  
 129 the global FAC and ionospheric equivalent current provided by the Active Magnetosphere  
 130 and Planetary Electrodynamics Response Experiment (AMPERE) (Anderson et al., 2000,  
 131 2002; Waters et al., 2001, 2020) and SuperMAG (Gjerloev, 2009, 2012), respectively. We use  
 132 data from 28 HSS/SIR storms with  $Dst \leq -50$  nT that occurred during 2010-2017 and use a  
 133 superposed epoch analysis to study the auroral current systems in the northern hemisphere.  
 134 Furthermore, as pointed out above, the dynamic pressure may affect the coupling between  
 135 the solar wind and magnetosphere. Therefore, we also study the effect of solar wind dynamic  
 136 pressure on the auroral current systems in the vicinity of the SIR.

137 The structure of the paper is as follows: section 2 describes the event selection process  
 138 and the data analysis methods. Section 3 shows the results in three parts: in 3.1 we analyse  
 139 all the events and investigate the spatial and temporal evolution of the field-aligned and  
 140 horizontal currents during the HSS/SIR driven storms, in 3.2, we separate the storms into  
 141 low and high SW dynamic pressure events and study its impact on the currents, and in 3.3  
 142 describe the correlation between the FACs, AE and Akasofu  $\varepsilon$ . Section 4 is a discussion of  
 143 the results and section 5 gives a summary and conclusion of our findings.

## 144 **2 Data, event selection and analysis method**

### 145 **2.1 Data**

146 Data from AMPERE, SuperMAG and the OMNIWeb have been used. The AMPERE  
 147 project provides fitted FAC densities in the high latitude region derived from magnetic field  
 148 perturbations measured onboard the Iridium Communication satellite constellation of more  
 149 than 70 satellites in near-polar orbit (Anderson et al., 2000, 2002; Waters et al., 2001, 2020).  
 150 SuperMAG provides gridded ground magnetic field perturbation vectors from magnetometer  
 151 measurements around the globe (Gjerloev, 2009, 2012; Waters et al., 2015). SuperMAG also  
 152 provides a list of substorm onsets derived from an automated algorithm using the SML index;  
 153 the SuperMAG equivalent of the AL index (Newell & Gjerloev, 2011b,a). The OMNIWeb  
 154 service provides data of the solar wind and geomagnetic indices (King & Papitashvili, 2005).  
 155 The Dst index is also taken from the OMNIWeb service. Since Dst is a 1 h index, all the  
 156 analysis and plots use the center of the 1 h window as a time tag.

157 Only data from the northern hemisphere is used. This is because there are less ground  
 158 magnetometer stations located in the southern hemisphere and the AMPERE FAC densities  
 159 may be less reliable due to the larger offset between the Earth's geomagnetic and geographic  
 160 south pole (e.g. Anderson et al., 2002), making the intersection point of Iridium satellite  
 161 orbits to often be in the southern auroral oval.

### 162 **2.2 Selecting HSS/SIR-driven geomagnetic storms**

163 The search for HSS/SIR-driven storms were limited to 2010 – 2017, as that is the period  
 164 when both AMPERE and SuperMAG have available coincident data. Events were selected  
 165 based on the geomagnetic storm criteria by Partamies et al. (2013) as described below.  
 166 Storms are typically categorised as weak ( $-50$  nT  $<$  Dst  $<$   $-30$  nT), moderate ( $-100$  nT  $<$   
 167 Dst  $<$   $-50$  nT) and strong (Dst  $<$   $-100$  nT) (Gonzalez et al., 1994; Loewe & Pröls, 1997,  
 168 e.g.). We only include storms that are moderate or strong. Therefore, we use the additional

169 condition that the Dst index must reach at least  $-50$  nT. The storm main phase onset time  
 170 was set to the time when the Dst index decreased below  $-15$  nT. The main phase ends when  
 171 the Dst index has reached a minimum. The recovery phase lasted from the Dst minimum  
 172 until the Dst index reached  $-15$  nT. In compound events where two or more storms follow  
 173 each by more than 60 h, but the Dst index does not manage to recover to  $-15$  nT, we truncate  
 174 the recovery phase of the 1st storm at the beginning of the 2nd storm, and include only the  
 175 1st storm in the analysis.

176 All the storms found using the above algorithm were compared with the HSS/SIR list  
 177 by Grandin et al. (2019), and only storms that had a main phase onset during the time of a  
 178 HSS/SIR event were selected. Grandin et al. (2019) in their HSS/SIR list removed any candi-  
 179 dates, which were likely affected by an ICME event by comparing the arrival time of the HSS  
 180 to ICME events from Richardson & Cane (2010) (<http://www.srl.caltech.edu/ACE/ASC/DATA/level3/icmetable2.l>).  
 181 In addition, we have used a more strict criteria for excluding potential ICME events. Any  
 182 storm that contained an ICME event and also those ICME events which had velocities  
 183 smaller than 500 km/s were removed. In total 140 storms with  $Dst \leq -50$  nT between 2010  
 184 and 2017 were identified, of which 46 were purely HSS/SIR-related. Of these 46 storms  
 185 there is full AMPERE data coverage for 28 storms, which form the dataset for our study.

186 Figure 1 shows the yearly distribution of the storms and the durations of the main and  
 187 recovery phases. The majority of the storms took place after 2015, during the declining  
 188 phase of solar cycle 24. Twenty-two of the 28 storms had a main phase duration of less than  
 189 10 h and the median duration was 6 h, with interpolated lower and upper quartiles of 4.5 h  
 190 and 9.5 h, respectively. In individual storms, the median recovery phase duration was 65 h  
 191 and the interpolated lower and upper quartiles were 36.5 h and 90.6 h, respectively.

192 Table 1 lists the main characteristics of the selected storms. The monthly distribution of  
 193 the storms peaked with seven storms in March followed by three in February, April, May and  
 194 September. The remaining months all had one or two storms, except for November that had  
 195 zero. Table 1 column 4 shows the spring/fall toward/away IMF sector polarity, indicating  
 196 whether the storm had a contribution of the Russell-McPherron effect following the “spring-  
 197 toward fall-away” (STFA) rule (Miyoshi & Kataoka, 2008). Here spring and autumn are  
 198 defined as the intervals spanning  $\pm 55$  days from the spring and autumn equinoxes (Zhao  
 199 & Zong, 2012). The S-T (spring-toward) and F-A (fall-away) labels indicate contribution  
 200 from the Russell-McPherron effect, while S-A (spring-away) and F-T (fall-toward) give no  
 201 contribution. The only equinox storm that had no contribution was storm #23, which  
 202 had F-T. In total, 23 of the 28 HSS/SIR storms, i.e. 82%, had a contribution from the  
 203 Russell-McPherron effect that increased the southward IMF  $B_z$  component.

204

## 205 **2.3 Data analysis methods**

206 The fitted AMPERE data products are provided at 2 minute cadence over a 10 min  
 207 window. We used the data at 10 minute temporal resolution, meaning all measurements  
 208 are independent. The spatial resolution is 1 h magnetic local time (MLT) and  $1^\circ$  magnetic  
 209 latitude (MLAT) in altitude adjusted corrected geomagnetic (AACGM) coordinates (Baker  
 210 & Wing, 1989). The gridded SuperMAG magnetic field perturbation vectors have 1 min  
 211 time resolution and spatial resolution is 1 MLT hour and  $2^\circ$  MLAT (Waters et al., 2015).  
 212 The OMNI SW and IMF data, mapped to the bowshock, have a time resolution of 1 h. The  
 213 data processing is described in the following subsections.

### 214 **2.3.1 Superposed epoch analysis**

215 The storm properties and auroral currents were studied using a superposed epoch anal-  
 216 ysis (SEA) approach. In SEA, the time series of a given parameter were overlapped using

Table 1: List of the 28 HSS/SIR storms in our study. Onset times are given in UT. The spring/fall toward/away column with blue text (S-T and F-A) have contributions from the Russell-McPherron effect and events with red text (F-T and S-A) do not have.

Storm number	Main phase onset (zero epoch)	Low/High P <sub>dyn</sub>	Spring/Fall Toward/Away	Main phase (h)	Recovery phase (h)	Dst minimum (nT)
1	02-May-2010 12:30	High	S-T	6	125	-71
2	04-Feb-2011 20:30	High	S-T	1	88	-63
3	01-Mar-2011 11:30	Low	S-T	3	60	-88
4	19-Feb-2012 00:30	Low	S-T	4	56	-63
5	12-Mar-2012 11:30	High	S-T	5	70	-54
6	26-Jan-2013 05:30	Low	S-T	17	30	-51
7	01-Mar-2013 09:30	High	S-T	1	50	-55
8	01-Jun-2013 02:30	High	–	6	86	-124
9	08-Dec-2013 04:30	High	–	4	22	-66
10	02-Mar-2015 02:30	Low	S-T	6	16	-54
11	15-Apr-2015 10:30	Low	S-T	37	35	-79
12	13-May-2015 01:30	High	S-T	5	42	-76
13	08-Jun-2015 06:30	Low	–	2	97	-73
14	04-Jul-2015 21:30	Low	–	8	75	-67
15	11-Sep-2015 08:30	Low	F-A	6	36	-81
16	07-Oct-2015 04:30	High	F-A	18	100	-124
17	16-Feb-2016 12:30	High	S-T	7	101	-57
18	06-Mar-2016 17:30	High	S-T	4	54	-98
19	02-Apr-2016 17:30	High	S-T	6	37	-56
20	12-Apr-2016 21:30	High	S-T	8	28	-55
21	08-May-2016 02:30	Low	S-T	6	93	-88
22	03-Aug-2016 05:30	Low	F-A	5	37	-52
23	23-Aug-2016 14:30	Low	F-T	7	34	-74
24	01-Sep-2016 02:30	Low	F-A	7	131	-59
25	28-Sep-2016 00:30	Low	F-A	33	79	-66
26	24-Oct-2016 00:30	Low	F-A	41	74	-59
27	01-Mar-2017 12:30	High	S-T	9	85	-61
28	27-Mar-2017 05:30	High	S-T	9	139	-74

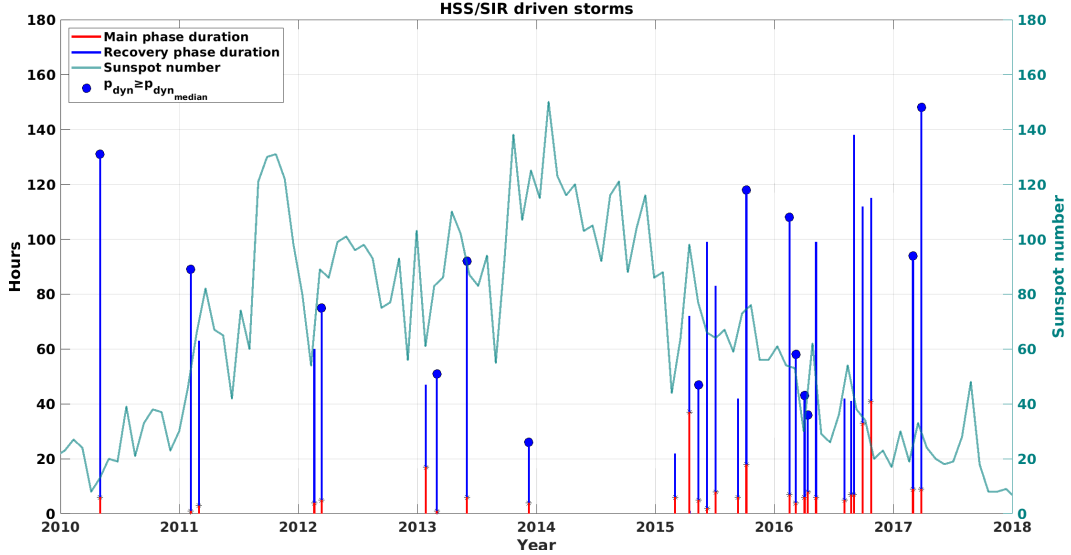


Figure 1: Distribution of the 28 HSS/SIR related storms. Red line shows the main phase duration of the storm and blue line the recovery phase duration (left axis). Storms with circles at the top of the lines are high dynamic pressure events (see section 3.2). The 27-day average sunspot number is also shown (right axis).

217 the same zero epoch time and then the median and quartiles were extracted. We used the  
 218 median and quartiles instead of mean and standard deviation as they are less affected by  
 219 outliers. The zero epoch ( $t_0$ ) was set to the onset of the storm’s main phase, defined as  
 220 the time when the Dst index first decreased to below  $-15$  nT (Partamies et al., 2013). The  
 221 choice of  $t_0$  can have implications on the characteristic behavior of the parameters being  
 222 studied (Ilie et al., 2008), and therefore it is important to choose an appropriate  $t_0$  for  
 223 the phenomena of interest. This study focuses on exploring both the temporal and spatial  
 224 variability of the field-aligned and ionospheric currents during the most active periods of  
 225 the HSS/SIR storms, and therefore choosing the storm main phase would reveal the general  
 226 evolution as the storm develops. In the SEA, the time window chosen was from 12 h before  
 227  $t_0$  until 60 h (2.5 days) afterwards. This time window includes information on the pre-storm  
 228 condition of the current systems and in the majority of the storms the activity level had  
 229 relaxed close to the normal time conditions within 2.5 days.

### 230 2.3.2 FACs from AMPERE

231 In order to reveal the spatial variation, hemispheric maps were constructed by super-  
 232 posing the currents at each MLAT/MLT grid cell, i.e. at each timestep the median value of  
 233 the 28 storms in each grid cell is shown:

$$J_{ij}(t) = \text{median}(J_{Nij}(t)), \quad \text{for } N = 1, 2, \dots, 28 \quad (1)$$

234 where  $t$  is the time from zero epoch,  $N$  is the storm number and  $i$  and  $j$  are the MLAT  
 235 and MLT coordinates, respectively.

236 In addition to the superposed maps, time series of the integrated FACs in each storm  
 237 and their superposition were also investigated. To maintain information about the upper

238 and lower quartiles of the integrated FAC, the upward and downward FAC densities were  
 239 processed separately for each storm:

$$J_{Nij}^+(t) = \begin{cases} J_{Nij}(t) & \text{if } J_{Nij}(t) > 0 \\ 0 & \text{else} \end{cases} \quad (2)$$

$$J_{Nij}^-(t) = \begin{cases} J_{Nij}(t) & \text{if } J_{Nij}(t) < 0 \\ 0 & \text{else} \end{cases} \quad (3)$$

240 where positive values represent the upward currents and negative values the downward  
 241 currents. When integrating the FACs, any current  $J$  with an absolute magnitude less than  
 242  $0.16 \mu\text{A}/\text{m}^2$  was set to zero. Anderson et al. (2014) found  $0.16 \mu\text{A}/\text{m}^2$  to be three times the  
 243 standard deviation of the quiet time current density. Therefore, by removing these small  
 244 currents, the integration only includes statistically significant FACs. The total upward or  
 245 downward integrated FAC for a given storm is:

$$I_N^\pm(t) = \sum_{i=\text{MLAT}} \sum_{j=\text{MLT}} A_{ij} J_{Nij}^\pm(t). \quad (4)$$

246 Here the FAC density was multiplied with the area of each grid cell,  $A_{ij}$ . The summation  
 247 was carried out from  $40^\circ$  to  $90^\circ$  MLAT and all MLTs. The grid sizes are  $1^\circ$  MLAT and 1 h  
 248 MLT. The timestep is 10 min and calculation was carried out between  $t_0 - 0.5$  d and  $t_0 + 2.5$   
 249 d. After the integrated FACs had been calculated for each event, they were added to SEA  
 250 to yield the total FAC versus SEA time.

251 Later, the total integrated currents were separated into four different MLT sectors,  
 252 noon (09-15 MLT), dusk (15-21 MLT), midnight (21-03 MLT) and dawn (03-09 MLT), to  
 253 allow for study of the behaviour in the different regions.

### 254 **2.3.3 Equivalent currents from SuperMAG**

255 The magnetic field vectors from SuperMAG were rotated clockwise by  $90^\circ$  to repre-  
 256 sent the horizontal equivalent currents. The units have not been converted from nT to A  
 257 to emphasize that we use the ground-magnetic perturbations. Gjerloev & Hoffman (2014)  
 258 reported an analysis of the SuperMAG data in a similar fashion, and pointed out a simple  
 259 relation between ground measured magnetic perturbation and current: 1 nTkm roughly cor-  
 260 responding to 2 A equivalent current (Kamide et al., 1982). Equivalent currents represent  
 261 the divergence-free part of the height-integrated current, which can often be approximated  
 262 as the Hall current. In the analysis of the electrojet currents, we separated the vectors  
 263 into southward and northward magnetic field perturbations, to represent the westward and  
 264 eastward horizontal currents, respectively. The integration was carried out from  $54 - 76^\circ$   
 265 MLAT across all included MLTs, then divided by the number of MLTs to show the average  
 266 eastward electrojet (EEJ) and westward electrojet (WEJ) current. In order to maintain  
 267 information about the upper and lower quartiles in the EEJ and WEJ currents, the inte-  
 268 gration and superposed epoch analysis was calculated separately for the different current  
 269 directions, similar to the upward and downward FACs discussed in Section 2.3.2.

### 270 **2.3.4 Solar wind parameters**

271 The SW and IMF parameters are delayed to the magnetospheric bowshock with 1 h  
 272 time resolution in the OMNI data base. Two additional quantities were derived using the  
 273 OMNI data, the solar wind dynamic pressure  $p_{\text{dyn}}$  and Akasofu  $\varepsilon$  parameter (Akasofu, 1981).  
 274 The solar wind dynamic pressure is:

$$P_{\text{dyn}} = m_p \rho_{\text{SW}} V_{\text{SW}}^2 \quad (5)$$

275 where  $m_p$  is the proton mass,  $\rho_{\text{SW}}$  is the upstream SW density and  $V_{\text{SW}}$  is the SW speed.  
 276 Akasofu  $\varepsilon$  is one of the most widely used coupling functions, describing energy coupling  
 277 between the solar wind and the magnetosphere. Akasofu  $\varepsilon$  is defined as:

$$\varepsilon(W) = \frac{4\pi}{\mu_0} V_{\text{SW}} B^2 \sin^4 \left( \frac{\theta}{2} \right) l_0 \quad (6)$$

278 where  $B$  is the IMF magnitude,  $\theta$  the IMF clock-angle and  $l_0$  the reconnection line at the  
 279 dayside magnetopause taken with the empirical value of  $7 R_E$  from Akasofu (1981).  
 280

### 281 3 Results

282 In this section, all the 28 storms are first studied together to examine what kind of  
 283 SW conditions and currents can be expected from a typical HSS/SIR driven storm. Then  
 284 the storms are split into two groups based on the SW dynamic pressure and the differences  
 285 in the SW driving, FACs and ionospheric currents are investigated. The last part of this  
 286 section focuses on the correlation between the FACs, AE index and solar wind coupling for  
 287 all the storms and the different dynamic pressure groups.

#### 288 3.1 Superposed epoch analysis of all HSS/SIR storms

289 Figure 2 shows the superposed SW OMNI data for all of the storms. The first three  
 290 panels are the SW dynamic pressure, velocity and density. These panels show that the  
 291 majority of the storms begin before the velocity reaches 500 km/s, during the time of large  
 292 plasma compression in the SIR. The following three panels show SW proton density, IMF  
 293  $B_Z$  component, IMF scalar value and Akasofu  $\varepsilon$  coupling function. Zero epoch (the time  
 294 when the Dst index decreases below  $-15$  nT) coincides with the minimum  $B_Z$  and maximum  
 295 IMF  $B$  magnitude. The negative  $B_Z$  is one of the important driving parameters allowing for  
 296 solar wind-magnetosphere coupling and increased SW density and IMF magnitude can be  
 297 associated with plasma compression in the SIR portion of the HSS. Last panel shows that  
 298 the coupling between the solar wind and magnetosphere starts to increase rapidly two hours  
 299 prior to  $t_0$  and reaches maximum at  $t_0$ , followed by a period of steady elevated coupling and  
 300 a second smaller peak 4 h after  $t_0$  (clearly visible in the upper quartile).

301 A polar MLT/MLAT overview of the superposed AMPERE FACs and SuperMAG  
 302 equivalent currents in the northern hemisphere at six different times are shown in Figure  
 303 3. The color shading shows the field-aligned upward (positive) and downward (negative)  
 304 current density, and the arrows show  $90^\circ$  rotated magnetic field perturbation vectors - red  
 305 arrows are eastward currents and blue arrows are westward currents. Panel a) is 12 h before  
 306  $t_0$  and shows the pre-storm condition of the FAC and electrojet currents, with very small  
 307 values. Panel b) is taken 2 h before  $t_0$ , and some enhancement can already be observed  
 308 in both the FACs and electrojets. The FAC enhancement is observed in all MLT sectors,  
 309 while all the equivalent currents above  $60^\circ$  MLAT are increased with the largest values in  
 310 the morning and evening sectors. The magnetic Harang discontinuity can be identified to  
 311 be located at 22 MLT below  $70^\circ$  MLAT, shifting westward by one MLT hour per  $2^\circ$  MLAT  
 312 up to  $74^\circ$ .

313 Panel c) shows that at  $t_0$ , major enhancements are observed in both the FAC and  
 314 electrojet currents, and the Harang discontinuity has moved to 21 MLT below  $68^\circ$  MLAT.  
 315 The spatial distribution of the FAC system displays the well known R1/R2 currents (Iijima

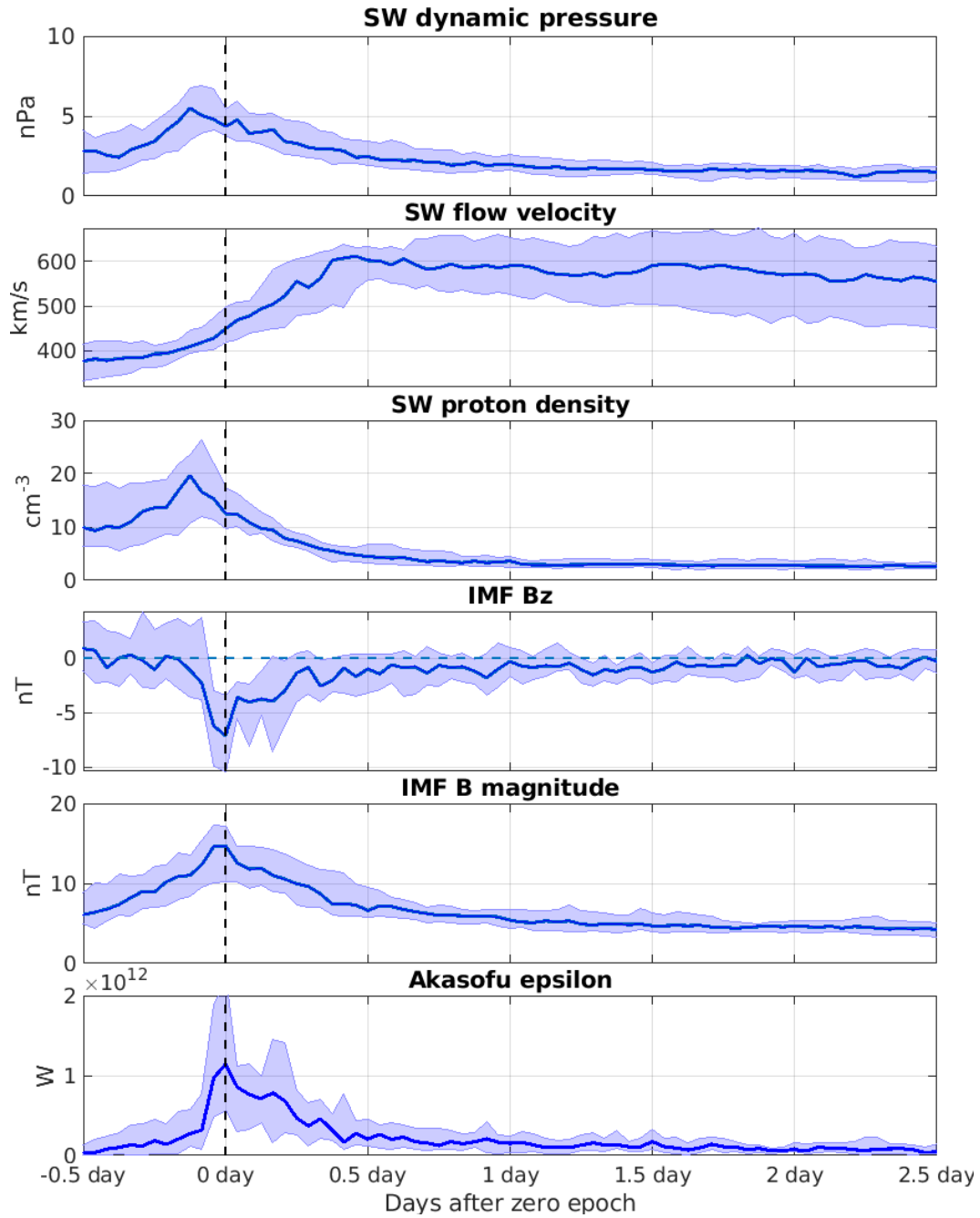


Figure 2: From top to bottom panel are the superposed solar wind dynamic pressure, flow velocity, density, northward IMF  $B_z$ -component, IMF B magnitude and Akasofu  $\epsilon$  for all the 28 storms in our study. The solid line shows the median superposed value and the shaded area indicates the upper and lower quartiles. The dashed vertical line shows the time of zero epoch.

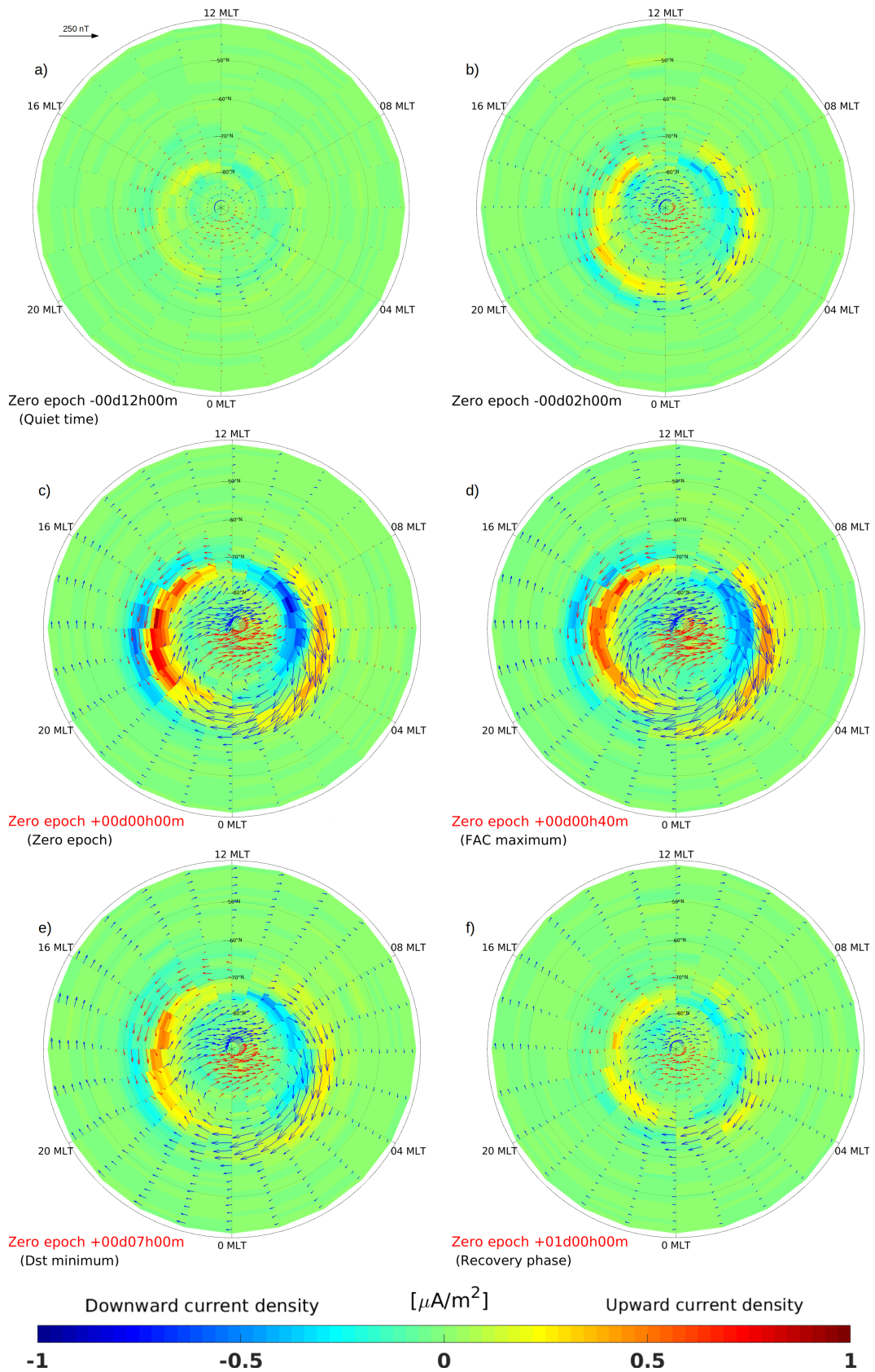


Figure 3: Superposed AMPERE FAC density and rotated SuperMAG magnetic field perturbation vectors for all the geomagnetic storms at six different times with respect to zero epoch plotted in AACGM coordinates.

316 & Potemra, 1978), with the polarward R1 oriented upward (downward) in dusk (dawn) and  
 317 the equatorward R2 currents having opposite directions than R1 in the same MLT sectors.  
 318 The maximum R1 current densities are observed at 17-18 MLT and at 68° MLAT (upward)  
 319 and at 07-08 MLT and 72° MLAT (downward). The WEJ has intensified and extended to  
 320 become dominant in the midnight sector.

321 Panel d) at  $t_0 + 40$  min shows the auroral currents at the time of maximum superposed  
 322 integrated FAC (determined from Figure 4 discussed below), and is 18 minutes earlier than  
 323 maximum superposed integrated horizontal equivalent currents that peak at  $t_0 + 58$  min. The  
 324 WEJ in the dawn and midnight sectors and the EEJ in the dusk sector are larger than at  
 325  $t_0$  and have expanded  $\sim 2^\circ$  further equatorwards. In the dusk sector enhancement in the  
 326 westward equivalent current is seen at mid-latitudes between 40–52° MLAT. These are likely  
 327 not real ionospheric currents, but disturbances from the asymmetric ring current and/or  
 328 magnetopause current that also increases during times of geomagnetic activity (Newell &  
 329 Gjerloev, 2012; Haaland & Gjerloev, 2013).

330 Panel e) shows the time of superposed Dst minimum and is the time the mid-latitude  
 331 disturbance maximizes. At this time the magnitudes of the FAC and equivalent currents  
 332 have reduced compared to panel d), but the extent of the WEJ in the midnight sector has  
 333 moved equatorward by  $\sim 4^\circ$  compared to  $t_0$ .

334 Panel f) is 24 h after  $t_0$ , in the middle of the recovery phase. The FAC and WEJ, but not  
 335 the EEJ, are still larger than at  $t_0 - 2$  h shown in panel b), with the Harang discontinuity still  
 336 at 21 MLT below 68° MLAT. The mid-latitude equivalent currents remain more prominent  
 337 24 h after  $t_0$  than what was seen in b) 2 h before  $t_0$ , and could therefore account for a  
 338 reduction in dusk side EEJ currents and slightly skew the Harang discontinuity westward  
 339 at the lower boundary of the auroral oval.

340 Figure 4 shows the superposed Dst index, the superposed AE, AU and AL indices, the  
 341 superposed integrated  $J_{eq}$  and the superposed total integrated FAC, separately for upward  
 342 and downward currents, with the number of substorm onsets from the SuperMAG onset list  
 343 (Newell & Gjerloev, 2011a). The superposed Dst index decreases in two steep slopes, with  
 344 the first spanning from  $t_0 - 1$  h until  $t_0 + 1$  h and the second from  $t_0 + 3$  h until the Dst  
 345 minimum at  $t_0 + 6$  h. The AE indices, integrated  $J_{eq}$  and integrated FAC start to show  
 346 signatures of enhancements  $\sim 3$  h before  $t_0$ , but experience rapid growth in the hour before  
 347  $t_0$ . The AE index and FAC reach respective maxima of 780 nT and 8.1 MA 35 min and  
 348 40 min after  $t_0$ , closely followed by a peak in the integrated westward  $J_{eq}$  58 min after  $t_0$ ,  
 349 almost 5 h before the Dst minimum.

350 Two hours after  $t_0$  the abrupt peak in the integrated FAC quickly decreases to 5.4  
 351 MA, before steadily increasing to reach a second and third maximum of 6.4 MA and 6.7  
 352 MA 4 h and 5 h 20 min after  $t_0$ ; the latter being around the time of Dst minimum. In  
 353 the integrated westward equivalent current the first and third peak occur 10 - 20 min after  
 354 the peaks in FACs, but are earlier in the second peak and quartiles. This slight difference  
 355 is likely attributed to changes in the ionospheric Hall conductivity, since the WEJ can be  
 356 assumed to have the main contribution from Hall currents. The number of substorm onsets  
 357 peak in the hour before  $t_0$ , with an average of 1.2 substorm onsets per hour per storm,  
 358 indicating high substorm activity and large variability in the electrojets. Newell & Gjerloev  
 359 (2011b) discussed the distribution of substorms detected by the algorithm and showed that,  
 360 although 4.4 h was the median separation between substorms, a large number of substorm  
 361 onsets were identified with less than 1 h separation, similar to what we often observe in the  
 362 storm main phase and particularly around storm onset.

363 The AL index and the integrated  $J_{eq}$  show similarities in the median value, but have  
 364 vastly different lower quartiles. In particular, the last peak in the main phase is clearly more  
 365 visible in the quartile of the integrated  $J_{eq}$ . This could be because the spatial coverage of  
 366 stations that contribute to the AL index is much more limited than that of the SuperMAG

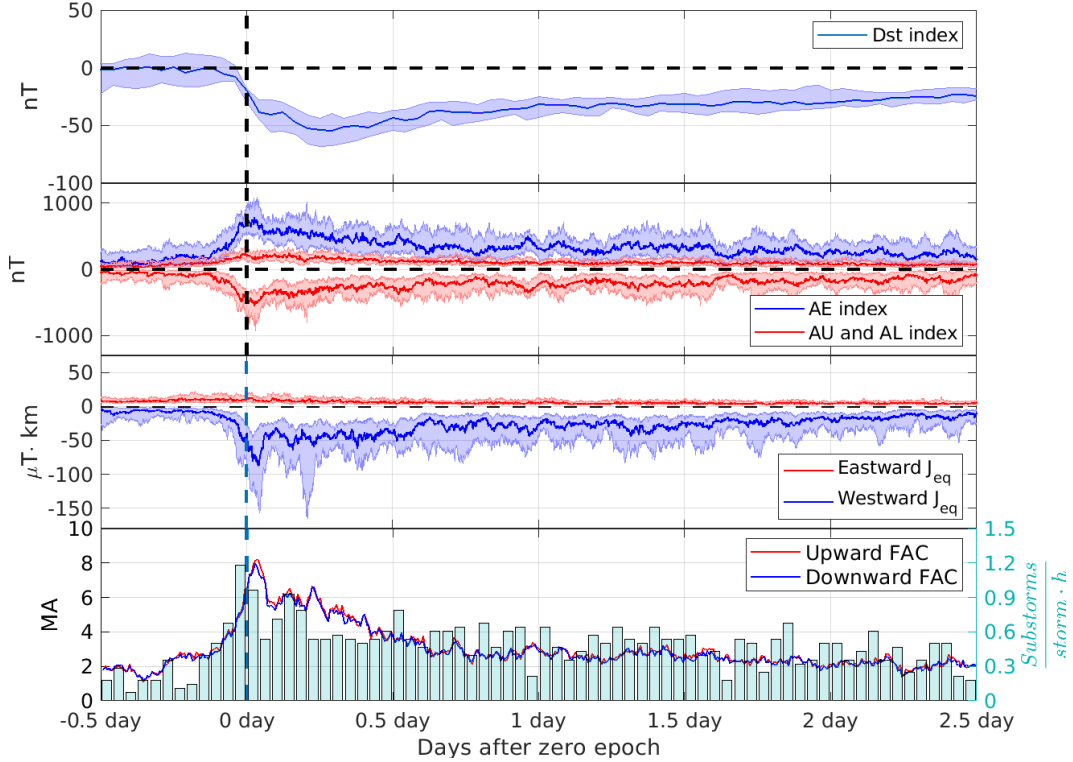


Figure 4: Top panel shows the superposed Dst index. The second panel is the superposed AE, AU and AL index. The third panel shows the superposed integrated SuperMAG  $J_{eq}$ . In the bottom panel is the total integrated FAC with bars showing the number of average substorm onsets pr storm occurring in 1-hour bins. The shaded areas shows the upper and lower quartiles of the superposed values.

367 network contributing to  $J_{eq}$ . In the storm recovery phase the currents and substorm activity  
 368 level appear to steadily decrease, but even 2.5 days after zero epoch there is still an enhanced  
 369 activity level compared to quiet time conditions.

370 Comparing the Dst index, substorm onsets and the integrated FAC and  $J_{eq}$ , it is clear  
 371 that the two steeper slopes in the Dst index during the storm main phase match the times  
 372 of peak substorm onsets followed by peaks in the integrated FAC and  $J_{eq}$ . McPherron et al.  
 373 (2018) observed large increases in the FAC and SML index following substorm onset, and  
 374 that substorm onset coincided with the time of largest solar wind-magnetosphere coupling.  
 375 This agrees with our observations that the largest solar wind driving occurs at the same  
 376 time as the peak in number of substorm onsets, followed by peaks in the currents. This  
 377 indicates that the maxima in the ionosphere currents take place during substorms and that  
 378 these times coincide with enhancements in the ring current observed in the Dst index.

379 The FACs and ionospheric current systems respond and behave differently depending  
 380 on magnetic local time (MLT). The integrated FACs are divided into four different MLT  
 381 sectors: noon (9 – 15 MLT), dusk (15 – 21 MLT), midnight (21 – 03 MLT) and dawn  
 382 (03 – 09 MLT) sector, as shown in Figure 5. The red (blue) line and shading show the  
 383 superposed value and the upper/lower quartiles of the upward (downward) integrated FAC.  
 384 Naturally, in the dusk (dawn) sector the upward (downward) current is R1 and vice versa  
 385 for R2. FACs in all sectors begin increasing slightly before  $t_0$ , but the dusk and dawn sectors  
 386 reach significantly larger peak values compared with the midnight and noon sectors. This is  
 387 expected, as the majority of R1 and R2 FACs are concentrated in dusk and dawn. The first

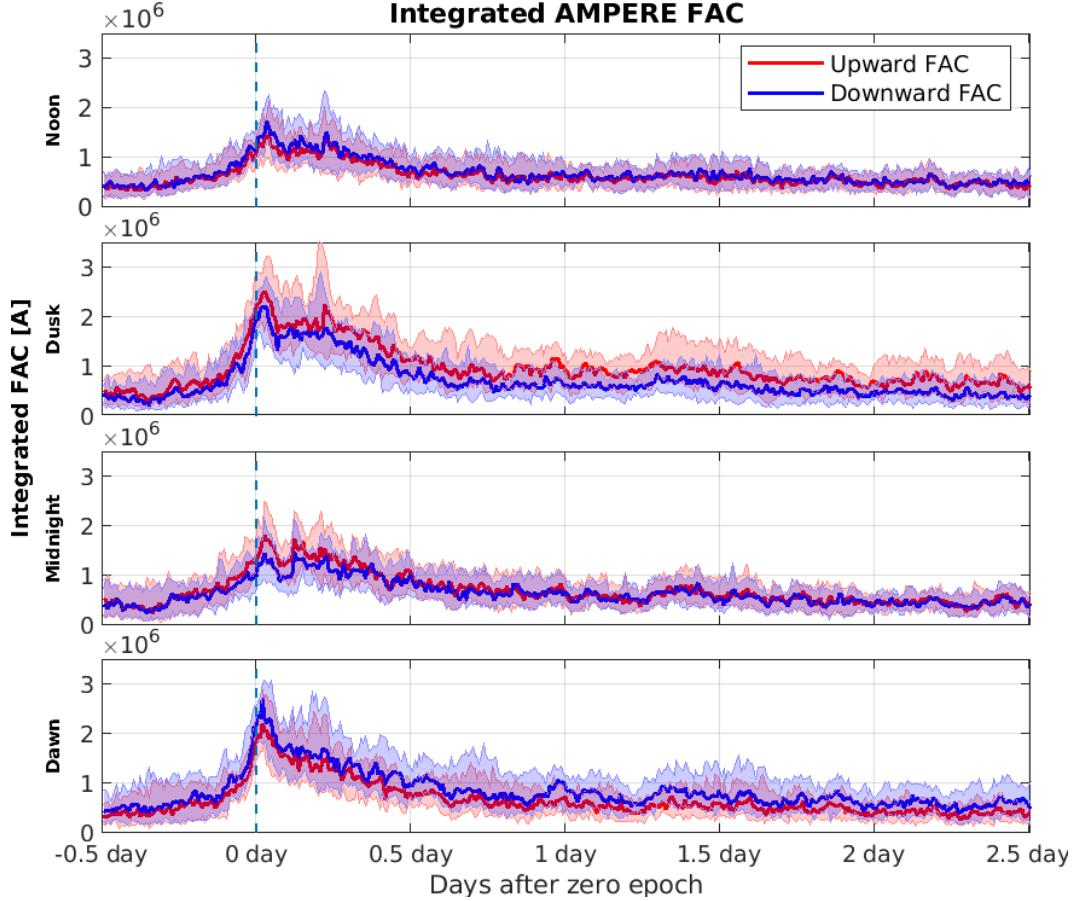


Figure 5: Superposed integrated FAC from AMPERE separated into four different MLT sectors.

388 FAC peak 40 min after  $t_0$  in Figure 4 is seen in all sectors. However, the second peak is only  
 389 seen in the median value of the noon and midnight sectors, although at the same time the  
 390 dusk sector has the largest value and there is some indication of a peak in the upper quartile  
 391 of the dusk and dawn sectors too. The third peak after 5 h 20 min is only clearly visible in  
 392 the median value of the noon and dusk sectors, but in the upper quartiles the third peak is  
 393 clearly visible in all sectors, and of larger magnitude than the first in noon and dusk. All in  
 394 all, the temporal behavior of R1 and R2 currents in different MLT sectors are very similar.

### 395 3.2 Effect of solar wind dynamic pressure on FACs and ionospheric currents

396 To study the effect of the SW dynamic pressure in the vicinity of the SIR, the 28  
 397 storms were split into groups of low and high  $p_{\text{dyn}}$ , denoted  $p_{\text{dyn}}^{\text{l}}$  and  $p_{\text{dyn}}^{\text{h}}$  respectively.  
 398 The division was based on the maximum SW dynamic pressure within  $\pm 3$  h from  $t_0$ . The  
 399 median maximum dynamic pressure in all of the events were 6.8 nPa, with a span from the  
 400 smallest being 2.6 nPa up to 15.7 nPa.

401 Table 2 summarizes the characteristics of the low and high pressure groups. The du-  
 402 rations of the main phase in the two categories are very similar and so are the median  
 403 minimum Dst at  $-66.5$  and  $-68.5$  nT for the  $p_{\text{dyn}}^{\text{l}}$  and  $p_{\text{dyn}}^{\text{h}}$  storms, respectively. Albeit the  
 404 similarities, the  $p_{\text{dyn}}^{\text{h}}$  storms are associated with substantially longer storm recovery phases

Table 2: Characteristics of low and high  $p_{\text{dyn}}$  storms

	Low	High
Number of storms	14	14
Median max $p_{\text{dyn}}$	5.1	9.3
Median min Dst	-66.5 nT	-68.5 nT
Min Dst in category	-88 nT	-124 nT
Median main phase duration	6.5 h	6.0 h
Median recovery phase duration	58.0 h	77.5 h
Median storm duration	67.5 h	82 h
Median time from HSS onset to $t_0$	26.5 h	12.5 h

405 with median of 58 h and 77.5 h for  $p_{\text{dyn}}^{\text{l}}$  and  $p_{\text{dyn}}^{\text{h}}$ , respectively, and the three largest events  
 406 measured by Dst minimum belongs to  $p_{\text{dyn}}^{\text{h}}$  storms.

407 Figure 6 accompanies Table 2 and shows the distribution of the Dst minimum and the  
 408 length of the storm main and recovery phase for both the  $p_{\text{dyn}}^{\text{l}}$  and  $p_{\text{dyn}}^{\text{h}}$  storms separately.  
 409 The top panel of Figure 6 shows a similar number of  $p_{\text{dyn}}^{\text{l}}$  and  $p_{\text{dyn}}^{\text{h}}$  storms in the smallest  
 410 Dst disturbance intervals from 50-64 nT and 65-79 nT, but the storms where Dst decreases  
 411 below  $-95$  nT are exclusively  $p_{\text{dyn}}^{\text{h}}$  storms. The middle panel shows the duration of the  
 412 main phase, where  $p_{\text{dyn}}^{\text{h}}$  storms are slightly favored amongst the storms with the shortest  
 413 main phase duration. The bottom panel shows the duration of the recovery phase, where  
 414  $p_{\text{dyn}}^{\text{l}}$  storms are strongly favored to have short storm recovery phases, while the opposite  
 415 is the case for  $p_{\text{dyn}}^{\text{h}}$  storms. Five of the storms have a recovery phase lasting  $\geq 100$  h,  
 416 of which one is among the  $p_{\text{dyn}}^{\text{l}}$  storms (#24) and six among the  $p_{\text{dyn}}^{\text{h}}$  storms (#1, 16, 17 and  
 417 28). There appears to be no relationship between the length of the recovery phase and the  
 418 minimum Dst reached.

419 From inspecting all of the 28 storms individually, none have Dst monotonically relaxing  
 420 back to quiet time condition in the recovery phase, but all of the storms have some time  
 421 intervals of further Dst decreases in the recovery phase. What appears to separate the storms  
 422 with the longest recovery phases from the rest is that the Dst decreases in the recovery phase  
 423 are larger and more frequent than in the other storms. This could indicate that  $p_{\text{dyn}}^{\text{h}}$  storms  
 424 are associated with more frequent and intense injections of particles into the ring current  
 425 during the recovery phase than  $p_{\text{dyn}}^{\text{l}}$  storms. However, the Akasofu  $\varepsilon$  describing solar wind  
 426 energy input into the magnetosphere is not higher during recovery phase of  $p_{\text{dyn}}^{\text{h}}$  as will  
 427 be seen from Figure 7. Alternatively, loss of ring current particles could be more efficient  
 428 during recovery phases of  $p_{\text{dyn}}^{\text{l}}$  compared with  $p_{\text{dyn}}^{\text{h}}$  storms. Wang et al. (2003) showed  
 429 that higher dynamic pressure during times of northward IMF orientation decreases the ring  
 430 current decay time, and as we will see in Figure 7, the  $p_{\text{dyn}}^{\text{l}}$  storms have a larger dynamic  
 431 pressure in the storm recovery phase than  $p_{\text{dyn}}^{\text{h}}$  events.

432 The toward and away IMF polarity of the events may also affect the duration of the  
 433 recovery phase (Miyoshi et al., 2007, 2013), as this allows for easier and more frequent  
 434 reconnection during the recovery phase via the Russell-McPherron effect. Table 1 showed  
 435 the season and IMF direction for all the storms. The  $p_{\text{dyn}}^{\text{l}}$  group contains 11 storms with  
 436 contribution from the Russell-McPherron effect, and the  $p_{\text{dyn}}^{\text{h}}$  group contains 12 storms with  
 437 contribution. Hence, both pressure groups are equally heavily influenced by the Russell-  
 438 McPherron effect, it is unlikely that it plays a significant role in the difference seen in the  
 439 recovery phase duration between the  $p_{\text{dyn}}^{\text{l}}$  and  $p_{\text{dyn}}^{\text{h}}$  storms.

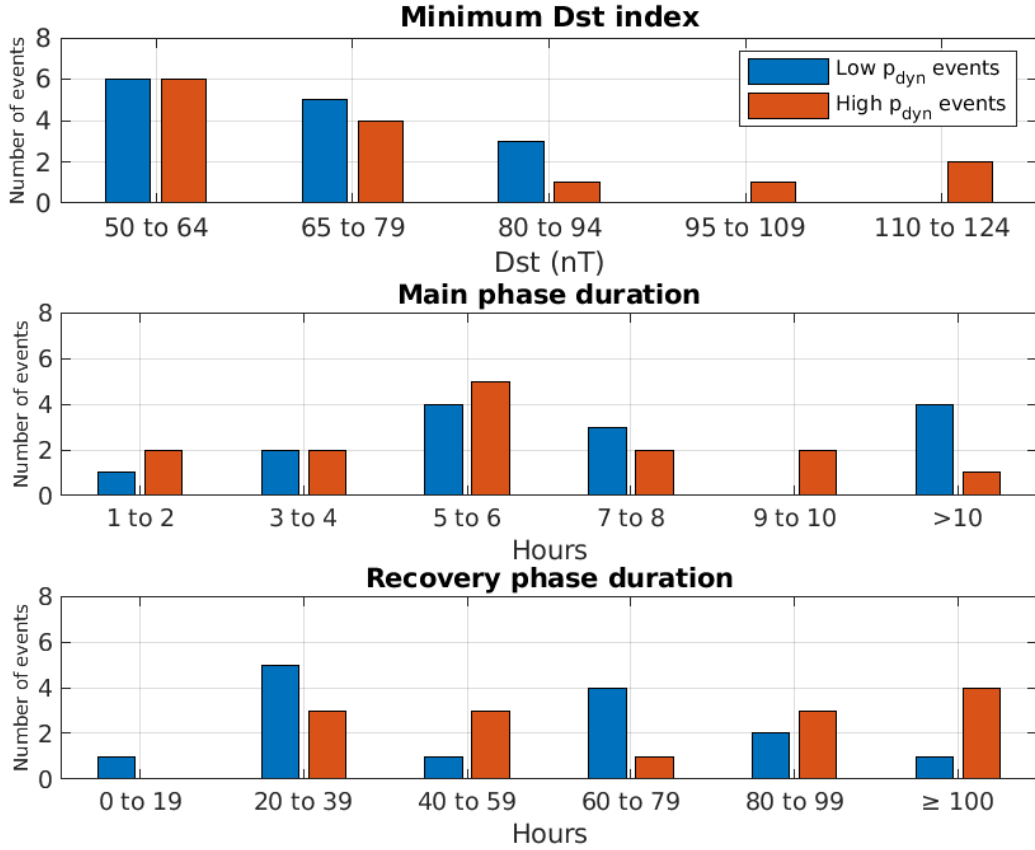


Figure 6: Distribution of minimum Dst and the length of storm main and recovery phase for the low and high  $p_{\text{dyn}}$  storms.

440 The IMF and SW conditions for both groups are shown in Figure 7. Two light vertical  
 441 dashed lines around the zero epoch show the interval used to select the  $p_{\text{dyn}}^{\text{l}}$  and  $p_{\text{dyn}}^{\text{h}}$   
 442 storms. The top panel shows the SW dynamic pressure where the  $p_{\text{dyn}}^{\text{h}}$  storms clearly  
 443 dominate around  $t_0$ , but as the pressure in the  $p_{\text{dyn}}^{\text{h}}$  storms decrease more rapidly because  
 444 of a much larger SW velocity, creating a greater rarefaction in its wake, the  $p_{\text{dyn}}^{\text{l}}$  storms  
 445 have the larger pressure from  $t_0 + 10$  h onwards. Second panel shows the SW flow velocity,  
 446 which shows that the  $p_{\text{dyn}}^{\text{l}}$  storms have a more steady and slightly higher flow velocity in  
 447 the hours before the  $t_0$ . At and after  $t_0$  the flow velocity of  $p_{\text{dyn}}^{\text{h}}$  storms exceed that in  $p_{\text{dyn}}^{\text{l}}$   
 448 storms, and reaches maximum within the first 12 hours before gradually decreasing. The  
 449 flow velocity of  $p_{\text{dyn}}^{\text{l}}$  storms behaves differently, having a much slower increase to maximum,  
 450 which is not reached within the first 2.5 days after  $t_0$ . The third panel shows the SW proton  
 451 density. Comparing  $p_{\text{dyn}}$  to SW velocity and density shows that the largest contribution  
 452 to  $p_{\text{dyn}}$  around the time of  $t_0$  comes from the density, although the higher flow velocity in  
 453 the  $p_{\text{dyn}}^{\text{h}}$  storms are likely indirectly responsible for this difference in the proton density at  
 454 the front of the SIRs. From  $t_0 + 8$  h onwards the  $p_{\text{dyn}}^{\text{l}}$  storms have a larger proton density  
 455 compared with the  $p_{\text{dyn}}^{\text{h}}$  storms. The fourth panel shows the  $B_Z$  component of the IMF.  $B_Z$   
 456 behaves very similarly in both categories, both in terms of timing, magnitude and variability.  
 457 This is likely because it is one of the main factors that makes the HSS/SIR geoeffective,  
 458 and any moderate or large storm ( $\text{Dst} \leq -50$  nT) requires a substantially negative  $B_Z$   
 459 component. The second last panel shows the IMF magnitude,  $B$ . As with the SW density,  
 460 the IMF magnitude is substantially larger in the  $p_{\text{dyn}}^{\text{h}}$  cases compared to the  $p_{\text{dyn}}^{\text{l}}$  around

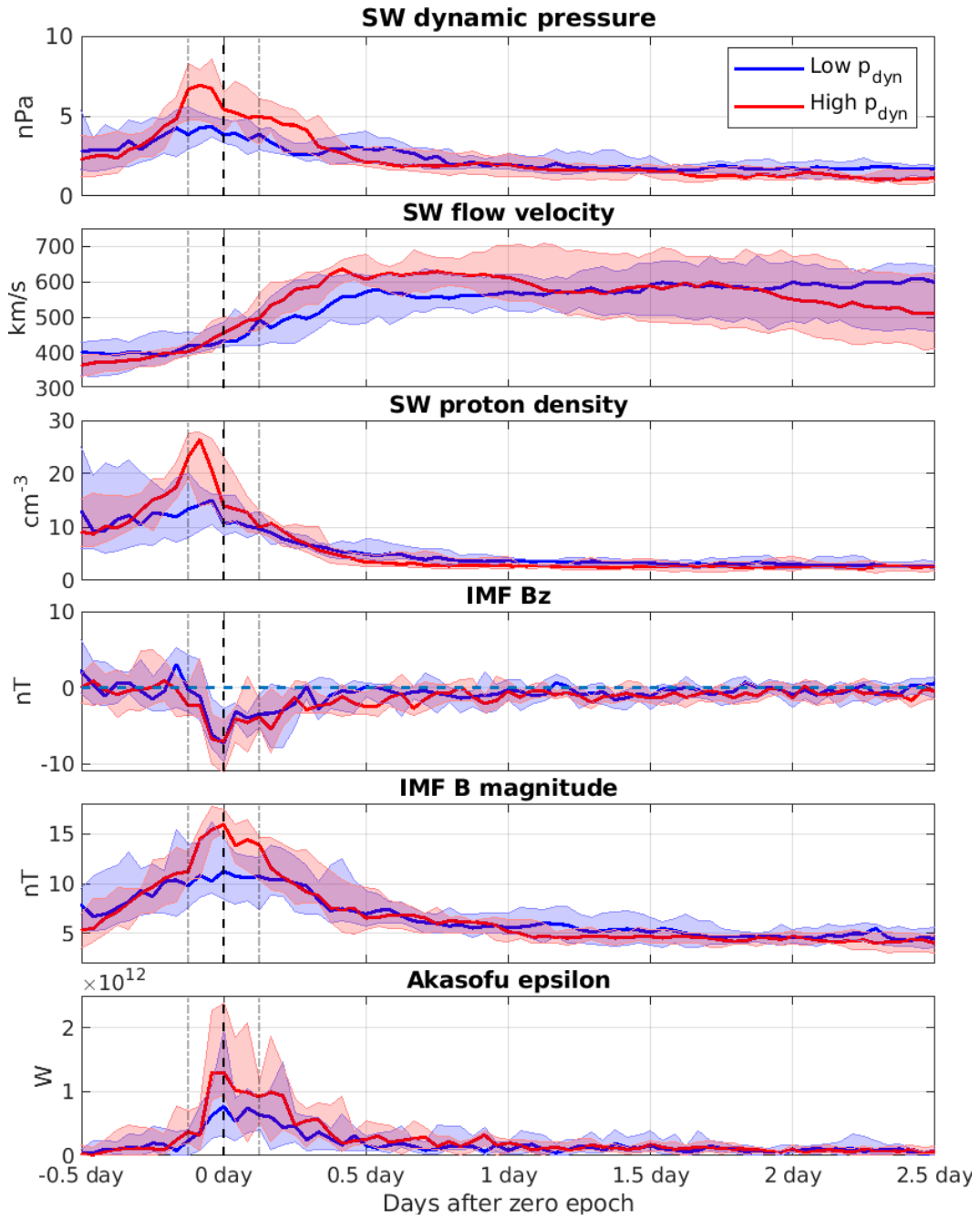


Figure 7: Solar wind parameters and Akasofu  $\epsilon$  for the low and high dynamic pressure storms. The blue (red) line is the low (high) pressure category and the shaded area shows the quartiles. The bold dashed vertical line shows the time of zero epoch, and the two faint dashed lines at  $\pm 3$  h enclose the time interval that the dynamic pressure categories were selected.

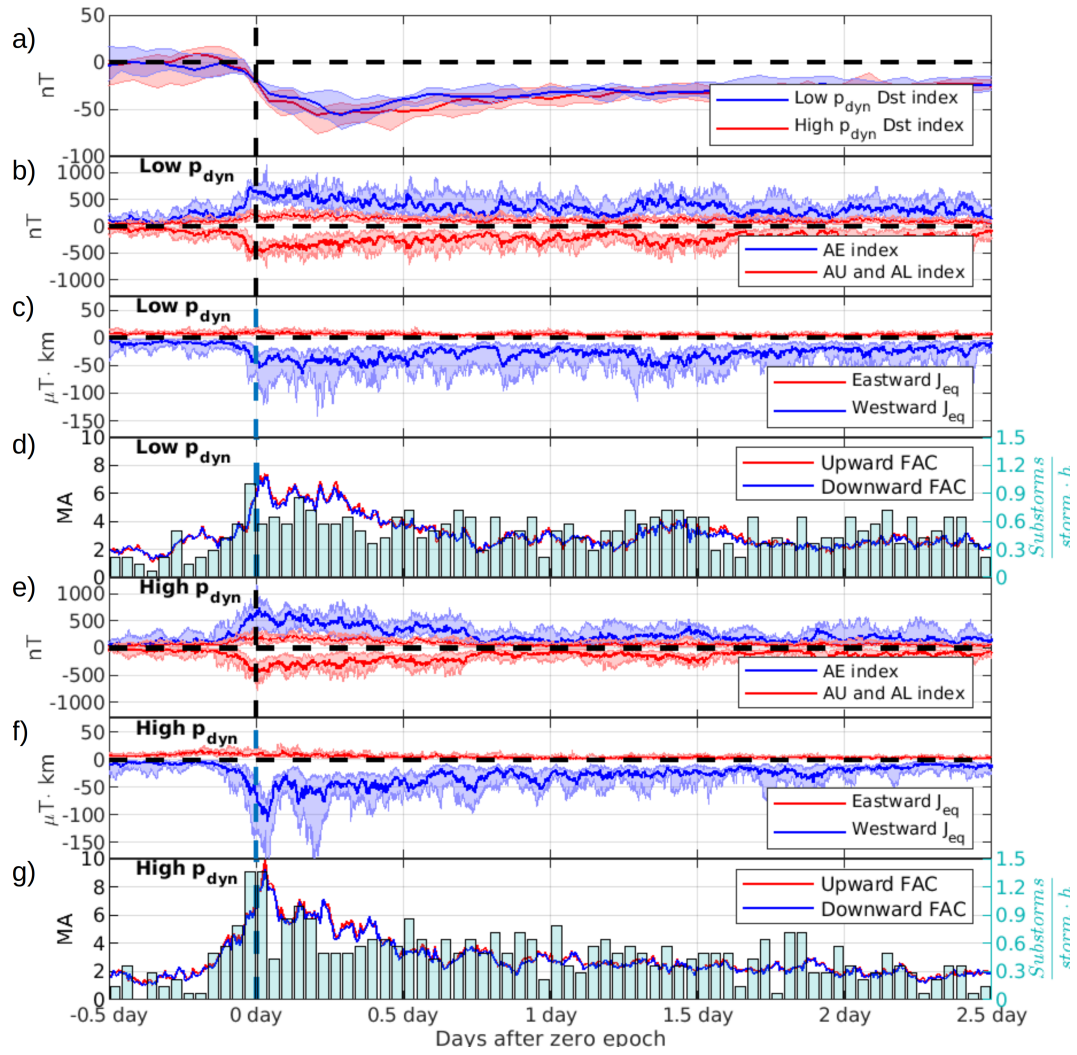


Figure 8: Same as Figure 4, but for low and high dynamic pressure storms.

461 the onset of the storm. This is also a signature of the compression of plasma and magnetic  
 462 field lines in the SIR portion of the HSS. Last panel shows the Akasofu coupling function  
 463 which indicates a larger SW-magnetosphere coupling for the  $p_{\text{dyn}}^{\text{h}}$  storms compared with the  
 464  $p_{\text{dyn}}^{\text{l}}$  storms in the storm main phase. In both groups the upper quartile shows two peaks  
 465 in coupling, one at  $t_0$  and another (smaller in the case of high  $p_{\text{dyn}}^{\text{h}}$ ) roughly 4 to 5 hours  
 466 later, with the  $p_{\text{dyn}}^{\text{h}}$  having larger energy transfer than  $p_{\text{dyn}}^{\text{l}}$  in both peaks.

467 Figure 8 shows the superposed Dst index, AE, AU and AL indices, integrated  $J_{\text{eq}}$   
 468 and the integrated FAC with number of substorm onsets for the  $p_{\text{dyn}}^{\text{l}}$  and  $p_{\text{dyn}}^{\text{h}}$  storms,  
 469 respectively. The Dst index in panel a) of the  $p_{\text{dyn}}^{\text{h}}$  storms show a slight positive excursion  
 470 three to six hours before  $t_0$ , which is an indication of storm sudden commencement (SSC)  
 471 (see e.g. Joselyn & Tsurutani, 1990). This feature is not visible in the  $p_{\text{dyn}}^{\text{l}}$  storms or in  
 472 Figure 4 where all storms were superposed. Following the storm onset, we see that the  
 473  $p_{\text{dyn}}^{\text{l}}$  storms have a slightly longer main phase than the  $p_{\text{dyn}}^{\text{h}}$  storms, with the superposed  
 474 Dst index reaching minimum 7 and 5 h after  $t_0$ , respectively. Also, the  $p_{\text{dyn}}^{\text{h}}$  storms have  
 475 a steeper decrease in Dst immediately after  $t_0$  that corresponds to a large increase and  
 476 maximum in both the AE index and integrated  $J_{\text{eq}}$  and FAC seen in panel e), f) and g).

477 The largest difference between the  $p_{\text{dyn}}^{\text{l}}$  and  $p_{\text{dyn}}^{\text{h}}$  storms occurs in the 3 hours before  
 478  $t_0$  until 2 hours afterwards. During this period both the AE indices, the integrated  $J_{\text{eq}}$   
 479 and FAC in the  $p_{\text{dyn}}^{\text{h}}$  storms are clearly larger and develop faster compared with the  $p_{\text{dyn}}^{\text{l}}$   
 480 storms. The first peak seen in the FAC of Figure 4 describing all storms comes primarily  
 481 from the  $p_{\text{dyn}}^{\text{h}}$  storms. Although the FAC in  $p_{\text{dyn}}^{\text{l}}$  also peak at this time, this maximum is  
 482 not significantly larger than the FAC throughout the rest of the storm main phase. The  
 483 maximum integrated  $J_{\text{eq}}$  is reached at the same time as maximum FAC for  $p_{\text{dyn}}^{\text{h}}$ , but is  
 484 later for  $p_{\text{dyn}}^{\text{l}}$  storms. The  $p_{\text{dyn}}^{\text{l}}$  reaches maximum  $J_{\text{eq}}$  3 h 45 min after  $t_0$ . In both groups  
 485  $\sim 90\%$  of the contribution to the  $J_{\text{eq}}$  during the storm main phase is from the westward  
 486  $J_{\text{eq}}$  current. For the  $p_{\text{dyn}}^{\text{h}}$  storms, there is a second peak in  $J_{\text{eq}}$  in the lower quartile during  
 487 the main phase, but this peak does not occur for all the storms in this category. The  $p_{\text{dyn}}^{\text{l}}$   
 488 storms remain at a high activity level throughout the main phase, and reach the last (4th)  
 489 peak at 6h 30 min after storm onset. Very little difference is seen in the AE indices between  
 490 the two groups in the main phase and early recovery phase, but from  $t_0 + 30$  h onwards the  
 491 AL index of  $p_{\text{dyn}}^{\text{l}}$  storms is continuously more intense.

492 The largest number of substorm onsets is seen in the hour before and after  $t_0$  for the  
 493  $p_{\text{dyn}}^{\text{h}}$  storms, with an average of 1.36 substorms per hour per storm. The  $p_{\text{dyn}}^{\text{l}}$  storms also  
 494 have a peak in number of substorm onsets in the hour before  $t_0$ , but a large drop in the hour  
 495 after  $t_0$  that agrees with the lower FAC and horizontal equivalent current activity compared  
 496 to the  $p_{\text{dyn}}^{\text{h}}$  storms. There is a second peak in the number of substorms in the latter half of  
 497 the main phase leading up to Dst minimum.

498 The auroral currents in both groups decrease steadily during the first 12 hours of the  
 499 storm recovery phase. From then on the activity level remains fairly constant and only  
 500 slowly continues decaying back to quiet time conditions. During the last interval of the  
 501 study window, from  $t_0 + 2$  d to  $t_0 + 2.5$  d, the number of substorm onsets, AE indices,  $J_{\text{eq}}$   
 502 and FAC are all larger in the  $p_{\text{dyn}}^{\text{l}}$  than  $p_{\text{dyn}}^{\text{h}}$  storms, which indicates some kind of reversed  
 503 situation from what was seen around the time of storm onset.

### 504 3.3 Solar wind-magnetosphere coupling, integrated FAC and AE index

505 In order to study how well the currents are predicted by the solar wind, the superposed  
 506 1 h averaged Akasofu  $\varepsilon$ , integrated FAC and AE index are shown in Figure 9. The top  
 507 panel shows all events together, the middle panel high pressure storms and the bottom  
 508 panel low pressure storms. The temporal evolution of the integrated FAC and AE index  
 509 follow the behaviour of the Akasofu  $\varepsilon$  very closely in all three panels, indicating that the  
 510 magnetosphere-ionosphere coupling during this period is to a large extent directly driven

Table 3: Correlation coefficients between Akasofu  $\varepsilon$ , AE and integrated FAC for the three groups (all storms, high  $p_{\text{dyn}}$  storms and low  $p_{\text{dyn}}$  storms) shown in Figure 9.

	All	Low	High
$r(\varepsilon, \text{AE})$	0.79	0.65	0.81
$r(\varepsilon, \text{FAC})$	0.90	0.83	0.89
$r(\text{AE}, \text{FAC})$	0.90	0.84	0.93

511 by the solar wind. Akasofu  $\varepsilon$  has a rapid increase starting 2 h before  $t_0$  for all storms and  
 512 the high pressure storms, and it precedes the integrated FAC and AE index by reaching  
 513 maximum 1 h earlier. After the storm main phase ends,  $\varepsilon$  drops off faster than the FAC  
 514 and AE index. The FAC and AE index follow closely each other and reach maxima of equal  
 515 relative magnitude in all three panels.

516 Even though the temporal behaviour of Akasofu  $\varepsilon$  and the currents are similar in Figure  
 517 11, the scaling factors between the low and high pressure storms are different, since for  $p_{\text{dyn}}^{\text{h}}$   
 518 storms the peak Akasofu  $\varepsilon$  is 1.3 TW and the peak FAC is 9.6 MA, while for  $p_{\text{dyn}}^{\text{l}}$  storms  
 519 the corresponding figures are 0.77 TW and 7.3 MA.

520 The superposed Dst index decreases in two intervals that both coincide with the times  
 521 of largest increase in the currents. Yokoyama & Kamide (1997) and Kamide, Yokoyama, et  
 522 al. (1998) also observed a two-peak structure in the energy injection to the ring current, in  
 523 the IMF  $B_Z$  and in the AE indices during the main phase of moderate and intense storms.  
 524 They suggested as one possible explanation that these features were associated with ICMEs,  
 525 and that the first peak occurring around the storm onset would be related to a compressed  
 526 southward oriented IMF (sheaths) and that the second peak just before Dst minimum was  
 527 caused by the southward IMF portion of the main ejecta or magnetic cloud. The storms in  
 528 this study are associated with HSS/SIR events and it is shown that the peaks are directly  
 529 driven by the solar wind coupling. The first peak in the Akasofu  $\varepsilon$  shortly after  $t_0$  is driven  
 530 by large compression in the SW IMF accompanied by southward  $B_Z$ , but the main driver of  
 531 the 2nd peak is not quite as obvious. By studying each term in the Akasofu  $\varepsilon$  individually  
 532 (plots not shown), the second peak seems to be driven by a combination of compressed IMF  
 533 and spikes in the  $\sin(\theta/2)^4$  term.

534 Table 3 shows the Pearson correlation coefficients in Figure 9 for all, low and high  
 535  $p_{\text{dyn}}$  storms. The highest overall correlation is found between AE and FAC in all the  
 536 groups, varying between 0.84 and 0.93. However, correlation between Akasofu  $\varepsilon$  and FAC is  
 537 almost as high, for all events 0.90 and slightly lower for  $p_{\text{dyn}}^{\text{l}}$  and  $p_{\text{dyn}}^{\text{h}}$ , with 0.83 and 0.89,  
 538 respectively. Correlation between Akasofu  $\varepsilon$  and AE is clearly smaller, though still high, for  
 539 all events 0.79 and for high  $p_{\text{dyn}}$  storms 0.81. The correlations are higher for  $p_{\text{dyn}}^{\text{h}}$  storms  
 540 than for the  $p_{\text{dyn}}^{\text{l}}$  storms. The correlation between Akasofu  $\varepsilon$  and AE estimated by Newell  
 541 et al. (2008) was 0.67, which is smaller than our 0.79 for all HSS/SIR events. However,  
 542 there are a few differences between our study and Newell et al. (2008). The correlation  
 543 analysis in this study used superposed data of HSS/SIR storms, meanwhile Newell et al.  
 544 (2008) included all solar wind conditions. High correlation between the AE indices and the  
 545 FACs have also been reported previously, e.g. Coxon et al. (2014a) found that correlation  
 546 coefficient between the R1 FAC and AL index was  $-0.83$  and between the R2 FAC and AL  
 547 index of  $-0.79$ .

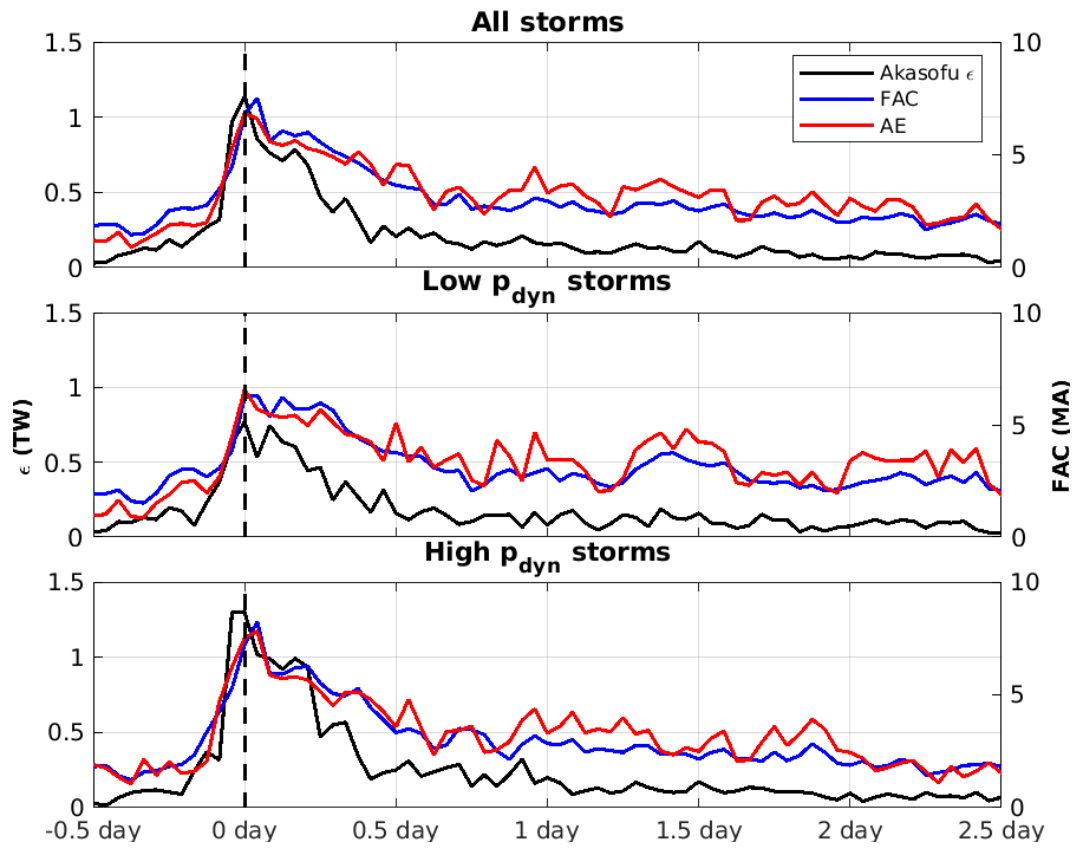


Figure 9: One hour averaged Akasofu  $\epsilon$ , total integrated FAC and AE index are plotted for all, low and high  $p_{\text{dyn}}$  storms.

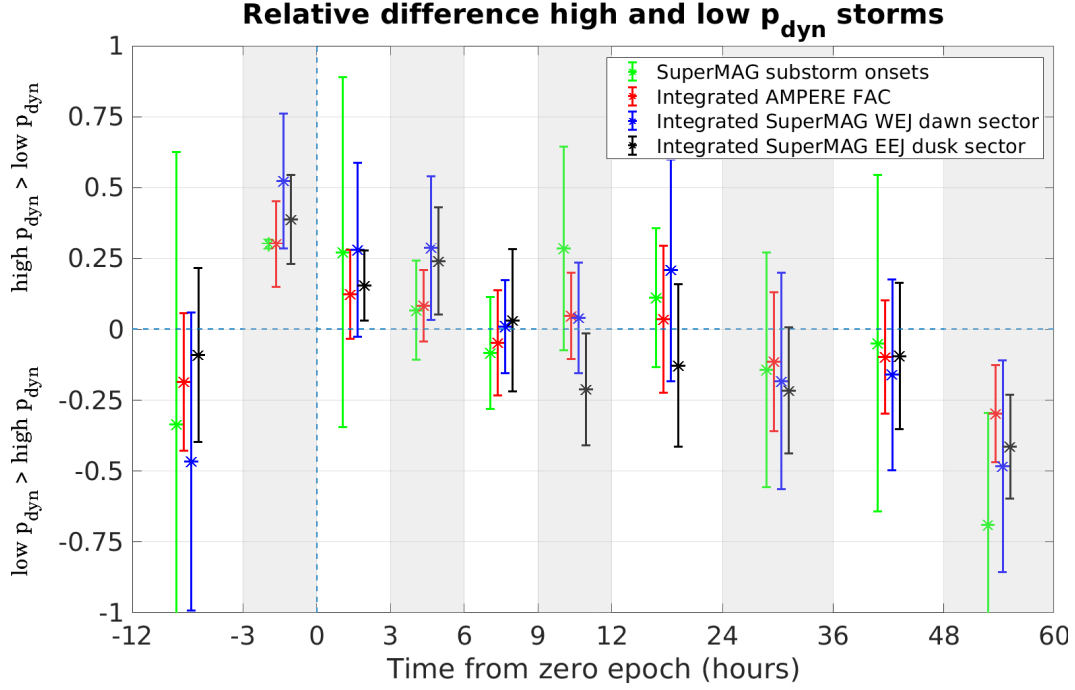


Figure 10: Relative difference between high and low  $p_{\text{dyn}}$  events for the data sets averaged over the white/grey shaded intervals - i.e. 9 h for the first interval containing the pre-onset conditions with the lowest activity, 3 h intervals from -3 h until 12 h after  $t_0$ . From 12 to 60 h after  $t_0$  the average relative difference is calculated over 12 h intervals.

#### 548 4 Discussion

549 Figure 10 is a summary of the relative difference between the  $p_{\text{dyn}}^{\text{h}}$  and  $p_{\text{dyn}}^{\text{l}}$  storms. The  
 550 AMPERE FAC and SuperMAG equivalent currents are averaged into 30 min bins before  
 551 calculating the relative difference:

$$\mu = \frac{1}{N} \sum_{i=1}^N \frac{x_i^{\text{h}} - x_i^{\text{l}}}{\frac{1}{2}(x_i^{\text{h}} + x_i^{\text{l}})} \quad (7)$$

and standard deviation as:

$$\sigma = \sqrt{\frac{1}{N} \sum_{i=1}^N \left( \frac{x_i^{\text{h}} - x_i^{\text{l}}}{\frac{1}{2}(x_i^{\text{h}} + x_i^{\text{l}})} - \mu \right)^2}. \quad (8)$$

552 Here  $x^{\text{l}}$  and  $x^{\text{h}}$  are the data sets (number of substorm onsets, integrated FAC and  
 553 integrated SuperMAG EEJ and WEJ currents) for low and high dynamic pressure storms,  
 554 respectively. The calculation is done over all the averaged data points  $N$  within each time  
 555 interval. The first time interval during the pre-storm conditions  $[t_0-12\text{h}, t_0-3\text{h}]$  (read as  
 556 “from  $t_0 - 12$  h to  $t_0 - 3$  h”) is 9 h,  $[t_0-3\text{h}, t_0+12]$  have 3 h intervals. In the storm recovery  
 557 phase from  $t_0+12\text{h}$  onwards the intervals are 12 h.

558 The difference between the high and low  $p_{\text{dyn}}$  condition is primarily seen just before  
 559 the storm onset and during the main phase, and in the late recovery phase. Larger  $p_{\text{dyn}}$

560 at the onset of the storm appear to induce a stronger magnetospheric response and more  
 561 rapid growth in the FAC and equivalent current system along with more substorm onsets.  
 562 Comparing the time intervals  $[t_0-3h, t_0]$  and  $[t_0, t_0+3h]$  in Figures 10 and 7, it is clear that  
 563 the larger intensity of the high  $p_{\text{dyn}}$  storms at this time coincides with increased solar wind  
 564 driving. During 3 h before the storm onset and during the storm main phase, currents and  
 565 number of substorms are higher for high  $p_{\text{dyn}}$  than low  $p_{\text{dyn}}$  storms. However, after one day  
 566 from the storm onset, the situation reverses, and 2 days after the onset in the late recovery  
 567 phase both currents and number of substorms are higher for low  $p_{\text{dyn}}$  than high  $p_{\text{dyn}}$  storms.  
 568 The only SW parameter that differs between the two groups at this time interval is the SW  
 569 flow velocity, with the low pressure storms having larger values (Figure 7, second panel).

570 Liu et al. (2019) found that the impact of SW  $p_{\text{dyn}}$  and  $E_Y$  on the mid/low latitude  
 571 ground magnetic perturbation  $\Delta H$  were largest on the dayside during the storm initial  
 572 phase due to the compression of the magnetopause and enhancement of the Chapman-  
 573 Ferraro current. In the main phase the  $\Delta H$  in all MLT sectors decreased, but with peaks  
 574 in the dusk sector and can explain the large westward equivalent currents we observe at  
 575 mid latitudes in Figure 3 after  $t_0$ . Le et al. (2020) showed that  $p_{\text{dyn}}$  plays a crucial role  
 576 in the intensity of major geomagnetic storms, and they argued that large and long lasting  
 577 southward IMF may alone not be sufficient if  $p_{\text{dyn}}$  is much lower than 3 nPa. In our study  
 578 the value dividing low and high pressure storms was 6.8 nPa.

579 The main focus of previous research relating the SW  $p_{\text{dyn}}$  to the magnetosphere-  
 580 ionosphere system has been on the low/mid-latitude region as the magnetic signatures there  
 581 are directly influenced by the Chapman-Ferraro and ring current. However, the R1 FACs  
 582 close partially through the Chapman-Ferraro current and the R2 FACs through the ring  
 583 current and are therefore closely connected to changes happening in these systems (Iijima  
 584 et al., 1990; Tsyganenko & Stern, 1996). Palmroth et al. (2004) found significant correlation  
 585 between increases in the SW  $p_{\text{dyn}}$  and ionospheric Joule heating at high latitudes, and  
 586 noted that the AE index increased by 35% 20 min after a pressure pulse during southward  
 587 IMF. This is of similar size to the changes that are seen in the AE index, integrated FACs  
 588 and equivalent currents between the high and low  $p_{\text{dyn}}$  events. The largest impact of the  
 589 dynamic pressure on the ionospheric currents occur in the beginning of the storm main  
 590 phase around the time of  $t_0$ . This is earlier than what was reported by Nakano et al. (2009),  
 591 who found high correlation between the  $p_{\text{dyn}}$  and R2 FAC during storm times when the  
 592 ring current was strongly enhanced. They speculated that the plasma pressure in the ring  
 593 current played a crucial part of the effect the SW  $p_{\text{dyn}}$  has on the magnetosphere and R2  
 594 currents.

595 From the SW and IMF data it is clear that the largest contribution to the dynamic  
 596 pressure comes from the SW density. This is expected as the majority of the HSS/SIR  
 597 storms develop in the SIR at the interface between the slow and high SW. Weigel (2010)  
 598 found by studying the evolution of the Dst index that the SW density modifies the solar  
 599 wind's geoefficiency to a greater degree than  $p_{\text{dyn}}$ , and that the influence on the geoefficiency  
 600 from increased SW density was smaller for larger storms. This agrees with our observations  
 601 as both  $p_{\text{dyn}}^l$  and  $p_{\text{dyn}}^h$  storms reach similar median Dst minima. It appears that  $p_{\text{dyn}}$  has  
 602 more profound impact on the way the storm develops and on the magnitude of auroral  
 603 currents during the first hour after storm onset.

604 Russell & McPherron (1973) stated that twice as many storms occur on average during  
 605 the equinoctial months compared to the solstitial months, and Echer et al. (2011) reported  
 606 a similar result from a study of all storms with peak Dst  $\leq -50$  nT from 1957 to 2008.  
 607 Here we find that 82% of moderate to large HSS/SIR storms with a Dst  $\leq -50$  nT have  
 608 contributions from the Russell-McPherron effect and occur  $\pm 55$  days from the equinoxes.  
 609 Although our study uses data from solar cycle 24 which was not included in Echer et al.  
 610 (2011), we see that for these HSS/SIR driven storms the Russell-McPherron effect seems to  
 611 play a more important role than in all storms studied by Echer et al. (2011) or Russell &  
 612 McPherron (1973).

## 5 Summary and conclusions

In this study, FACs and ionospheric equivalent currents in HSS/SIR driven storms have been analysed using AMPERE and SuperMAG data. To be included, storms needed to have  $\text{Dst} \leq -50$  nT and occur during a HSS/SIR event listed by Grandin et al. (2019). In total, 46 HSS/SIR driven storms were detected during the years 2010 – 2017, with full data coverage available for 28 storms, which were selected for this study (Table 2). To our knowledge, this is the first statistical superposed epoch analysis (SEA) study of global FACs and horizontal currents behaviour during HSS/SIR-driven storms.

The storms were analyzed using SEA with zero epoch ( $t_0$ ) centered at the onset of the main phase, which was in this study defined as the time when the Dst index decreased below -15 nT. The evolution and distribution of FACs and horizontal equivalent currents in the entire high latitude ( $\geq 40^\circ$  MLAT) northern hemisphere have been studied. The storms were also separated into low and high dynamic pressure events, denoted  $p_{\text{dyn}}^{\text{l}}$  and  $p_{\text{dyn}}^{\text{h}}$ , respectively, based on the solar wind dynamic pressure values within  $\pm 3$  h of  $t_0$ . When looking at solar wind parameters, this time interval roughly corresponds to the SIR portion of the HSS, containing compressed solar wind plasma ahead of the high-speed flows.

The main findings are:

- Moderate to strong HSS/SIR storms tend to begin when the SIR with enhanced solar wind density and compressed magnetic field with  $B_Z$  pointing in the southward direction interacts with the magnetopause.
- Twenty-three of 28, i.e. 82% of all storms have contributions from the Russell-McPherron effect in increasing the IMF southward  $B_Z$  component in the GSM coordinate system. Both the low and high  $p_{\text{dyn}}$  storms have about equally many storms that are affected by the Russell-McPherron effect.
- For high  $p_{\text{dyn}}$  events, the solar wind velocity maximum is reached earlier than for low  $p_{\text{dyn}}$  events. Also, the lead times to storm onset is shorter for high than low  $p_{\text{dyn}}$  events (12.5 h and 26.5 h, respectively).
- The superposed Dst minimum for all the storms is  $-54$  nT and occurs 6 h after the storm onset time. When separated into  $p_{\text{dyn}}^{\text{l}}$  and  $p_{\text{dyn}}^{\text{h}}$  storms, no significant difference is found between the superposed minimum Dst value, but the main phase duration is slightly shorter for high pressure storms than low pressure storms, with durations of 5 and 7 h, respectively.
- Typically only the  $p_{\text{dyn}}^{\text{h}}$  events show a signature of a SSC before the storm onset, have profoundly longer storm recovery phase duration (median of 77.5 h and 58 h for  $p_{\text{dyn}}^{\text{h}}$  and  $p_{\text{dyn}}^{\text{l}}$  storms, respectively) and contain the three largest events measured by minimum Dst.
- The integrated currents have three peaks in the main phase. In the upward and downward FACs, the first and most intense peak of 8.1 MA occurs in the early main phase ( $t_0 + 40$  min), a smaller peak of 6.4 MA in the middle of the main phase ( $t_0 + 4$ h) and a slightly larger peak of 6.7 MA occurs just before Dst minimum ( $t_0 + 5$  h 20 min) at the end of the main phase. At the same times, the equivalent currents peak and there are large spikes in the lower quartile of the WEJ current at the time of the first and third peaks.
- The first peak in the FAC is seen both in low and high  $p_{\text{dyn}}$ , but in high  $p_{\text{dyn}}$  category the peak is higher with a maximum FAC of 9.6 MA.
- Substorm onsets peak one hour before  $t_0$  for both  $p_{\text{dyn}}^{\text{l}}$  and  $p_{\text{dyn}}^{\text{h}}$  storms. Since  $t_0$  is the time when Dst has dropped below  $-15$  nT, this indicates that substorms commence at about the same time as the storm starts to develop. A second peak in the number of substorm onsets (1-h resolution data) is seen in association with the second FAC peak for both low and high  $p_{\text{dyn}}$ .
- In the main phase the Dst index decreases in two intervals at the same time as the number of substorm onsets peak and currents are increasing towards their peak values.

Hence, it appears that particle injections into the ring current take place in association with substorm onsets and intensifications of the ionospheric R1/R2 current systems. It is assumed that also substorm current wedges are formed, but it is not possible to extract those from the spatially and temporally superposed data.

- The temporal evolution of HSS/SIR-driven storms is very strongly driven by the solar wind. The Akasofu  $\varepsilon$  parameter (1-h resolution) has a similar temporal behaviour as the FACs have for both  $p_{\text{dyn}}^{\text{l}}$  and  $p_{\text{dyn}}^{\text{h}}$  events. The SW-magnetosphere coupling is considerably larger for high than low  $p_{\text{dyn}}$  storms in the main phase (peak values 1.3 TW and 0.77 TW, respectively). For  $p_{\text{dyn}}^{\text{h}}$  storms, Akasofu  $\varepsilon$  has a large peak at the storm onset, while for  $p_{\text{dyn}}^{\text{l}}$  storms the peak at the onset is not as pronounced.
- In the storm recovery phase, Akasofu  $\varepsilon$  decreases to pre-storm time conditions, but the currents as well as the number of substorm onsets still remain high, and higher for  $p_{\text{dyn}}^{\text{l}}$  than  $p_{\text{dyn}}^{\text{h}}$  storms. After about 2 days from the storm onset, the number of substorm onsets becomes clearly higher for low than high  $p_{\text{dyn}}$  events. At this time, solar wind velocity and the dynamic pressure become higher for  $p_{\text{dyn}}^{\text{l}}$  than  $p_{\text{dyn}}^{\text{h}}$  events, indicating that solar wind velocity in the recovery phase may play an important role in substorm generation.
- The strong driving of the ionosphere by the solar wind is also evidenced by the high correlation coefficient between the Akasofu  $\varepsilon$  and FAC, which is 0.90, and between Akasofu  $\varepsilon$  and AE, 0.79. Not surprisingly, the correlation coefficient between the ionospheric parameters AE and FAC is also very high, 0.90.
- All the correlation coefficients are higher for the superposed  $p_{\text{dyn}}^{\text{h}}$  storms than for the superposed  $p_{\text{dyn}}^{\text{l}}$  storms. This is likely due to the fact that  $p_{\text{dyn}}^{\text{h}}$  storms have significantly higher Akasofu  $\varepsilon$  values than  $p_{\text{dyn}}^{\text{l}}$  during the storm main phase. The correlation coefficient between the AE index and FAC is 0.93 for  $p_{\text{dyn}}^{\text{h}}$  storms.

## Acknowledgments

This work was supported by the Academy of Finland project 314664 and 314670. We thank the AMPERE team and the AMPERE Science Center for providing the Iridium derived data products (<http://ampere.jhuapl.edu/index.html>). For the ground magnetometer data and substorm onset list we gratefully thank the SuperMAG collaboration and all organizations involved (<https://supermag.jhuapl.edu/info/>). For the geomagnetic indices, solar wind and interplanetary magnetic field data we gratefully thank NASA/GSFC's Space Physics Data Facility's OMNIWeb (<https://omniweb.gsfc.nasa.gov/>). All data used in this study can be accessed through the links given above. We would also like to thank Dr. Ari Viljanen for insightful discussions and constructive comments on the manuscript.

## References

- Akasofu, S.-I. (1981). Energy coupling between the solar wind and the magnetosphere. *Space Science Reviews*, 28(2), 121–190. doi: <https://doi.org/10.1007/BF00218810>
- Anderson, B., Korth, H., Waters, C., Green, D., Merkin, V., Barnes, R., & Dyrud, L. (2014). Development of large-scale birkeland currents determined from the active magnetosphere and planetary electrodynamics response experiment. *Geophysical Research Letters*, 41(9), 3017–3025. doi: <https://doi.org/10.1002/2014GL059941>
- Anderson, B., Korth, H., Waters, C., Green, D., & Stauning, P. (2008). Statistical birkeland current distributions from magnetic field observations by the iridium constellation. In *Annales geophysicae* (Vol. 26, pp. 671–687). doi: <https://doi.org/10.5194/angeo-26-671-2008>
- Anderson, B., Ohtani, S.-I., Korth, H., & Ukhorskiy, A. (2005). Storm time dawn-dusk asymmetry of the large-scale birkeland currents. *Journal of Geophysical Research: Space Physics*, 110(A12). doi: <https://doi.org/10.1029/2005JA011246>
- Anderson, B., Takahashi, K., Kamei, T., Waters, C., & Toth, B. (2002). Birkeland current

- 715 system key parameters derived from iridium observations: Method and initial validation  
716 results. *Journal of Geophysical Research: Space Physics*, 107(A6), SMP–11. doi: <https://doi.org/10.1029/2001JA000080>  
717
- 718 Anderson, B., Takahashi, K., & Toth, B. A. (2000). Sensing global birkeland currents  
719 with iridium® engineering magnetometer data. *Geophysical Research Letters*, 27(24),  
720 4045–4048. doi: <https://doi.org/10.1029/2000GL000094>
- 721 Baker, K., & Wing, S. (1989). A new magnetic coordinate system for conjugate studies at  
722 high latitudes. *Journal of Geophysical Research: Space Physics*, 94(A7), 9139–9143. doi:  
723 <https://doi.org/10.1029/JA094iA07p09139>
- 724 Balogh, A., Gosling, J., Jokipii, J., Kallenbach, R., & Kunow, H. (1999). *Corotating*  
725 *interaction regions* (Vol. 7). Springer Science & Business Media.
- 726 Belcher, J., & Davis Jr, L. (1971). Large-amplitude alfvén waves in the interplanetary  
727 medium, 2. *Journal of Geophysical Research*, 76(16), 3534–3563. doi: <https://doi.org/10.1029/JA076i016p03534>  
728
- 729 Borovsky, J. E., & Denton, M. H. (2006). Differences between cme-driven storms and cir-  
730 cled storms. *Journal of Geophysical Research: Space Physics*, 111(A7). doi: <https://doi.org/10.1029/2005JA011447>  
731
- 732 Boudouridis, A., Zesta, E., Lyons, L., Anderson, P., & Lummerzheim, D. (2004). Magneto-  
733 spheric reconnection driven by solar wind pressure fronts.  
734 doi: <https://doi.org/10.5194/angeo-22-1367-2004>
- 735 Boudouridis, A., Zesta, E., Lyons, L., Anderson, P., & Lummerzheim, D. (2005). Enhanced  
736 solar wind geoeffectiveness after a sudden increase in dynamic pressure during southward  
737 imf orientation. *Journal of Geophysical Research: Space Physics*, 110(A5). doi: <https://doi.org/10.1029/2004JA010704>  
738
- 739 Boudouridis, A., Zesta, E., Lyons, R., Anderson, P., & Lummerzheim, D. (2003). Effect of  
740 solar wind pressure pulses on the size and strength of the auroral oval. *Journal of Geo-*  
741 *physical Research: Space Physics*, 108(A4). doi: <https://doi.org/10.1029/2002JA009373>
- 742 Burns, A., Solomon, S., Qian, L., Wang, W., Emery, B., Wiltberger, M., & Weimer, D.  
743 (2012). The effects of corotating interaction region/high speed stream storms on the  
744 thermosphere and ionosphere during the last solar minimum. *Journal of atmospheric and*  
745 *solar-terrestrial physics*, 83, 79–87. doi: <https://doi.org/10.1016/j.jastp.2012.02.006>
- 746 Coxon, J., Milan, S., Clausen, L., Anderson, B., & Korth, H. (2014b). A superposed  
747 epoch analysis of the regions 1 and 2 birkeland currents observed by ampere during  
748 substorms. *Journal of Geophysical Research: Space Physics*, 119(12), 9834–9846. doi:  
749 <https://doi.org/10.1002/2014JA020500>
- 750 Coxon, J., Milan, S. E., Clausen, L. B. N., Anderson, B. J., & Korth, H. (2014a). The  
751 magnitudes of the regions 1 and 2 birkeland currents observed by ampere and their role in  
752 solar wind-magnetosphere-ionosphere coupling. *Journal of Geophysical Research: Space*  
753 *Physics*, 119(12), 9804–9815. doi: <https://doi.org/10.1002/2014JA020138>
- 754 Dungey, J. W. (1961). Interplanetary magnetic field and the auroral zones. *Physical Review*  
755 *Letters*, 6(2), 47. doi: <https://doi.org/10.1103/PhysRevLett.6.47>
- 756 Echer, E., Gonzalez, W., & Tsurutani, B. (2011). Statistical studies of geomagnetic storms  
757 with peak  $dst \leq -50$  nt from 1957 to 2008. *Journal of Atmospheric and Solar-Terrestrial*  
758 *Physics*, 73(11-12), 1454–1459. doi: <https://doi.org/10.1016/j.jastp.2011.04.021>
- 759 Gjerloev, J. (2009). A global ground-based magnetometer initiative. *Eos, Transactions*  
760 *American Geophysical Union*, 90(27), 230–231. doi: <https://doi.org/10.1029/2009EO270002>  
761
- 762 Gjerloev, J. (2012). The supermag data processing technique. *Journal of Geophysical*  
763 *Research: Space Physics*, 117(A9). doi: <https://doi.org/10.1029/2012JA017683>
- 764 Gjerloev, J., & Hoffman, R. (2014). The large-scale current system during auroral substorms.  
765 *Journal of Geophysical Research: Space Physics*, 119(6), 4591–4606. doi: <https://doi.org/10.1002/2013JA019176>  
766
- 767 Gonzalez, W. D., Joselyn, J. A., Kamide, Y., Kroehl, H. W., Rostoker, G., Tsurutani, B. T.,  
768 & Vasyliunas, V. M. (1994). What is a geomagnetic storm? *Journal of Geophysical*

- 769 *Research: Space Physics*, 99(A4), 5771–5792. doi: 10.1029/93JA02867
- 770 Gonzalez, W. D., Tsurutani, B. T., & De Gonzalez, A. L. C. (1999). Interplanetary origin  
771 of geomagnetic storms. *Space Science Reviews*, 88(3-4), 529–562. doi: [https://doi.org/](https://doi.org/10.1023/A:1005160129098)  
772 10.1023/A:1005160129098
- 773 Gosling, J. T., Asbridge, J., Bame, S., & Feldman, W. (1978). Solar wind stream interfaces.  
774 *Journal of Geophysical Research: Space Physics*, 83(A4), 1401–1412. doi: [https://doi](https://doi.org/10.1029/JA083iA04p01401)  
775 [.org/10.1029/JA083iA04p01401](https://doi.org/10.1029/JA083iA04p01401)
- 776 Grandin, M., Aikio, A. T., & Kozlovsky, A. (2019). Properties and geoeffectiveness of  
777 solar wind high-speed streams and stream interaction regions during solar cycles 23 and  
778 24. *Journal of Geophysical Research: Space Physics*, 124(6), 3871–3892. doi: [https://](https://doi.org/10.1029/2018JA026396)  
779 [doi.org/10.1029/2018JA026396](https://doi.org/10.1029/2018JA026396)
- 780 Haaland, S., & Gjerloev, J. (2013). On the relation between asymmetries in the ring current  
781 and magnetopause current. *Journal of Geophysical Research: Space Physics*, 118(12),  
782 7593–7604. doi: 10.1002/2013JA019345
- 783 Iijima, T., Potemra, T., & Zanetti, L. (1990). Large-scale characteristics of magnetospheric  
784 equatorial currents. *Journal of Geophysical Research: Space Physics*, 95(A2), 991–999.  
785 doi: <https://doi.org/10.1029/JA095iA02p00991>
- 786 Iijima, T., & Potemra, T. A. (1978). Large-scale characteristics of field-aligned currents  
787 associated with substorms. *Journal of Geophysical Research: Space Physics*, 83(A2),  
788 599–615. doi: <https://doi.org/10.1029/JA083iA02p00599>
- 789 Ilie, R., Liemohn, M. W., Thomsen, M. F., Borovsky, J. E., & Zhang, J. (2008). Influence  
790 of epoch time selection on the results of superposed epoch analysis using ace and mpa  
791 data. *Journal of Geophysical Research: Space Physics*, 113(A3). doi: [https://doi.org/](https://doi.org/10.1029/2008JA013241)  
792 [10.1029/2008JA013241](https://doi.org/10.1029/2008JA013241)
- 793 Jian, L., Russell, C., Luhmann, J., & Skoug, R. (2006). Properties of stream interactions  
794 at one au during 1995–2004. *Solar Physics*, 239(1-2), 337–392. doi: [https://doi.org/](https://doi.org/10.1007/s11207-006-0132-3)  
795 [10.1007/s11207-006-0132-3](https://doi.org/10.1007/s11207-006-0132-3)
- 796 Joselyn, J., & Tsurutani, B. (1990). Geomagnetic sudden impulses and storm sudden  
797 commencements: A note on terminology. *Eos, Transactions American Geophysical Union*,  
798 71(47), 1808–1809. doi: <https://doi.org/10.1029/90EO00350>
- 799 Juusola, L., Kauristie, K., Amm, O., & Ritter, P. (2009). Statistical dependence of auroral  
800 ionospheric currents on solar wind and geomagnetic parameters from 5 years of champ  
801 satellite data. In *Annales geophysicae* (Vol. 27, pp. 1005–1017). doi: [https://doi.org/](https://doi.org/10.5194/angeo-27-1005-2009)  
802 [10.5194/angeo-27-1005-2009](https://doi.org/10.5194/angeo-27-1005-2009)
- 803 Kamide, Y., Ahn, B.-H., Akasofu, S.-I., Baumjohann, W., Friis-Christensen, E., Kroehl, H.,  
804 ... others (1982). Global distribution of ionospheric and field-aligned currents during  
805 substorms as determined from six ims meridian chains of magnetometers: Initial results.  
806 *Journal of Geophysical Research: Space Physics*, 87(A10), 8228–8240. doi: [https://](https://doi.org/10.1029/JA087iA10p08228)  
807 [doi.org/10.1029/JA087iA10p08228](https://doi.org/10.1029/JA087iA10p08228)
- 808 Kamide, Y., Baumjohann, W., Daglis, I., Gonzalez, W., Grande, M., Joselyn, J., ...  
809 others (1998b). Current understanding of magnetic storms: Storm-substorm relation-  
810 ships. *Journal of Geophysical Research: Space Physics*, 103(A8), 17705–17728. doi:  
811 <https://doi.org/10.1029/98JA01426>
- 812 Kamide, Y., Baumjohann, W., Daglis, I. A., Gonzalez, W. D., Grande, M., Joselyn, J. A., ...  
813 Vasyliunas, V. M. (1998a). Current understanding of magnetic storms: Storm-substorm  
814 relationships. *Journal of Geophysical Research: Space Physics*, 103(A8), 17705–17728.  
815 doi: 10.1029/98JA01426
- 816 Kamide, Y., Yokoyama, N., Gonzalez, W., Tsurutani, B. T., Daglis, I. A., Brekke, A., &  
817 Masuda, S. (1998). Two-step development of geomagnetic storms. *Journal of Geophysical*  
818 *Research: Space Physics*, 103(A4), 6917–6921. doi: <https://doi.org/10.1029/97JA03337>
- 819 King, J., & Papitashvili, N. (2005). Solar wind spatial scales in and comparisons of hourly  
820 wind and ace plasma and magnetic field data. *Journal of Geophysical Research: Space*  
821 *Physics*, 110(A2). doi: <https://doi.org/10.1029/2004JA010649>

- 822 Korth, H., Anderson, B., & Waters, C. (2010). Statistical analysis of the dependence of  
823 large-scale birkeland currents on solar wind parameters. *Annales Geophysicae (09927689)*,  
824 *28*(2). doi: <https://doi.org/10.5194/angeo-28-515-2010>
- 825 Krieger, A., Timothy, A., & Roelof, E. (1973). A coronal hole and its identification as  
826 the source of a high velocity solar wind stream. *Solar Physics*, *29*(2), 505–525. doi:  
827 <https://doi.org/10.1007/BF00150828>
- 828 Laundal, K. M., Reistad, J. P., Finlay, C. C., Østgaard, N., Tenfjord, P., Snekvik, K., &  
829 Ohma, A. (2018). Interplanetary magnetic field bx component influence on horizontal and  
830 field-aligned currents in the ionosphere. *Journal of Geophysical Research: Space Physics*,  
831 *123*(5), 3360–3379. doi: <https://doi.org/10.1002/2017JA024864>
- 832 Le, G.-M., Liu, G.-A., & Zhao, M.-X. (2020). Dependence of major geomagnetic storm  
833 intensity ( $dst \leq -100$  nt) on associated solar wind parameters. *Solar Physics*, *295*(8),  
834 1–9. doi: <https://doi.org/10.1007/s11207-020-01675-3>
- 835 Liu, B.-J., Zhang, X.-X., He, F., & Zong, Q.-G. (2019). The magnetic local time distribu-  
836 tion of storm geomagnetic field disturbance under different conditions of solar wind and  
837 interplanetary magnetic field. *Journal of Geophysical Research: Space Physics*, *124*(4),  
838 2656–2667. doi: <https://doi.org/10.1029/2018JA026287>
- 839 Lockwood, M., Owens, M. J., Barnard, L. A., Haines, C., Scott, C. J., McWilliams, K. A.,  
840 & Coxon, J. C. (2020). Semi-annual, annual and universal time variations in the mag-  
841 netosphere and in geomagnetic activity: 1. geomagnetic data. *Journal of Space Weather*  
842 *and Space Climate*, *10*, 23. doi: <https://doi.org/10.1051/swsc/2020023>
- 843 Loewe, C., & Prölss, G. (1997). Classification and mean behavior of magnetic storms.  
844 *Journal of Geophysical Research: Space Physics*, *102*(A7), 14209–14213. doi: <https://doi.org/10.1029/96JA04020>
- 845
- 846 McPherron, R., Anderson, B., & Chu, X. (2018). Relation of field-aligned currents measured  
847 by the network of iridium® spacecraft to solar wind and substorms. *Geophysical Research*  
848 *Letters*, *45*(5), 2151–2158. doi: <https://doi.org/10.1002/2017GL076741>
- 849 Miyoshi, Y., & Kataoka, R. (2008). Flux enhancement of the outer radiation belt electrons  
850 after the arrival of stream interaction regions. *Journal of Geophysical Research: Space*  
851 *Physics*, *113*(A3). doi: <https://doi.org/10.1029/2007JA012506>
- 852 Miyoshi, Y., Kataoka, R., Kasahara, Y., Kumamoto, A., Nagai, T., & Thomsen, M. (2013).  
853 High-speed solar wind with southward interplanetary magnetic field causes relativistic  
854 electron flux enhancement of the outer radiation belt via enhanced condition of whistler  
855 waves. *Geophysical Research Letters*, *40*(17), 4520–4525. doi: <https://doi.org/10.1002/grl.50916>
- 856
- 857 Miyoshi, Y., Morioka, A., Kataoka, R., Kasahara, Y., & Mukai, T. (2007). Evolution of the  
858 outer radiation belt during the november 1993 storms driven by corotating interaction  
859 regions. *Journal of Geophysical Research: Space Physics*, *112*(A5). doi: <https://doi.org/10.1029/2006JA012148>
- 860
- 861 Nakano, S., Ueno, G., Ohtani, S., & Higuchi, T. (2009). Impact of the solar wind dynamic  
862 pressure on the region 2 field-aligned currents. *Journal of Geophysical Research: Space*  
863 *Physics*, *114*(A2). doi: <https://doi.org/10.1029/2008JA013674>
- 864 Neupert, W. M., & Pizzo, V. (1974). Solar coronal holes as sources of recurrent geomagnetic  
865 disturbances. *Journal of Geophysical Research*, *79*(25), 3701–3709. doi: <https://doi.org/10.1029/JA079i025p03701>
- 866
- 867 Newell, P., & Gjerloev, J. (2011a). Evaluation of supermag auroral electrojet indices  
868 as indicators of substorms and auroral power. *Journal of Geophysical Research: Space*  
869 *Physics*, *116*(A12). doi: <https://doi.org/10.1029/2011JA016779>
- 870 Newell, P., & Gjerloev, J. (2011b). Substorm and magnetosphere characteristic scales  
871 inferred from the supermag auroral electrojet indices. *Journal of Geophysical Research:*  
872 *Space Physics*, *116*(A12). doi: <https://doi.org/10.1029/2011JA016936>
- 873 Newell, P., & Gjerloev, J. W. (2012). Supermag-based partial ring current indices. *Journal*  
874 *of Geophysical Research: Space Physics*, *117*(A5). doi: [10.1029/2012JA017586](https://doi.org/10.1029/2012JA017586)

- 875 Newell, P., Sotirelis, T., Liou, K., & Rich, F. (2008). Pairs of solar wind-magnetosphere  
876 coupling functions: Combining a merging term with a viscous term works best. *Journal of Geophysical Research: Space Physics*, *113*(A4). doi: <https://doi.org/10.1029/2007JA012825>  
877  
878
- 879 Palmroth, M., Pulkkinen, T., Janhunen, P., McComas, D., Smith, C., & Koskinen, H.  
880 (2004). Role of solar wind dynamic pressure in driving ionospheric joule heating. *Journal of Geophysical Research: Space Physics*, *109*(A11). doi: <https://doi.org/10.1029/2004JA010529>  
881  
882
- 883 Partamies, N., Juusola, L., Tanskanen, E., & Kauristie, K. (2013). Statistical properties of  
884 substorms during different storm and solar cycle phases. *Annales Geophysicae (09927689)*,  
885 *31*(2). doi: <https://doi.org/10.5194/angeo-31-349-2013>  
886
- 887 Richardson, I. G., & Cane, H. V. (2010). Near-earth interplanetary coronal mass ejections  
888 during solar cycle 23 (1996–2009): Catalog and summary of properties. *Solar Physics*,  
889 *264*(1), 189–237. doi: <https://doi.org/10.1007/s11207-010-9568-6>  
890
- 891 Richardson, I. G., & Cane, H. V. (2012). Solar wind drivers of geomagnetic storms during  
892 more than four solar cycles. *Journal of Space Weather and Space Climate*, *2*, A01. doi:  
893 <https://doi.org/10.1051/swsc/2012001>  
894
- 895 Rostoker, G., & Fälthammar, C.-G. (1967). Relationship between changes in the inter-  
896 planetary magnetic field and variations in the magnetic field at the earth's surface.  
897 *Journal of Geophysical Research*, *72*(23), 5853–5863. doi: <https://doi.org/10.1029/JZ072i023p05853>  
898
- 899 Russell, C., & McPherron, R. (1973). Semiannual variation of geomagnetic activity. *Journal*  
900 *of geophysical research*, *78*(1), 92–108. doi: <https://doi.org/10.1029/JA078i001p00092>  
901
- 902 Tanskanen, E., Snekvik, K., Slavin, J., Pérez-Suárez, D., Viljanen, A., Goldstein, M., ...  
903 Mursula, K. (2017). Solar cycle occurrence of alfvénic fluctuations and related geo-  
904 efficiency. *Journal of Geophysical Research: Space Physics*, *122*(10), 9848–9857. doi:  
905 <https://doi.org/10.1002/2017JA024385>  
906
- 907 Tsurutani, B. T., & Gonzalez, W. D. (1987). The cause of high-intensity long-duration  
908 continuous ae activity (hildcaas): Interplanetary alfvén wave trains. *Planetary and Space*  
909 *Science*, *35*(4), 405–412. doi: [https://doi.org/10.1016/0032-0633\(87\)90097-3](https://doi.org/10.1016/0032-0633(87)90097-3)  
910
- 911 Tsurutani, B. T., Gonzalez, W. D., Gonzalez, A. L., Guarnieri, F. L., Gopalswamy, N.,  
912 Grande, M., ... others (2006). Corotating solar wind streams and recurrent geomagnetic  
913 activity: A review. *Journal of Geophysical Research: Space Physics*, *111*(A7). doi:  
914 <https://doi.org/10.1029/2005JA011273>  
915
- 916 Tsyganenko, N. A., & Stern, D. P. (1996). Modeling the global magnetic field of the  
917 large-scale birkeland current systems. *Journal of Geophysical Research: Space Physics*,  
918 *101*(A12), 27187–27198. doi: <https://doi.org/10.1029/96JA02735>  
919
- 920 Turner, N. E., Cramer, W. D., Earles, S. K., & Emery, B. A. (2009). Geoefficiency and energy  
921 partitioning in cir-driven and cme-driven storms. *Journal of Atmospheric and Solar-*  
922 *Terrestrial Physics*, *71*(10-11), 1023–1031. doi: [https://doi.org/10.1016/j.jastp.2009.02](https://doi.org/10.1016/j.jastp.2009.02.005)  
923 .005
- 924 Wang, C., Chao, J., & Lin, C.-H. (2003). Influence of the solar wind dynamic pressure  
925 on the decay and injection of the ring current. *Journal of Geophysical Research: Space*  
926 *Physics*, *108*(A9). doi: <https://doi.org/10.1029/2003JA009851>  
927
- 928 Waters, C., Anderson, B., Green, D. L., Korth, H., Barnes, R. J., & Vanhamäki, H. (2020).  
Science data products for ampere. In M. W. Dunlop & H. Lühr (Eds.), *Ionospheric multi-*  
*spacecraft analysis tools: Approaches for deriving ionospheric parameters* (pp. 141–165).  
Cham: Springer International Publishing. doi: [10.1007/978-3-030-26732-2\\_7](https://doi.org/10.1007/978-3-030-26732-2_7)
- 929 Waters, C., Anderson, B., & Liou, K. (2001). Estimation of global field aligned currents  
930 using the iridium® system magnetometer data. *Geophysical Research Letters*, *28*(11),  
931 2165–2168. doi: <https://doi.org/10.1029/2000GL012725>  
932
- 933 Waters, C., Gjerloev, J., Dupont, M., & Barnes, R. (2015). Global maps of ground magne-  
934 tometer data. *Journal of Geophysical Research: Space Physics*, *120*(11), 9651–9660. doi:  
935 <https://doi.org/10.1002/2015JA021596>  
936

- 929 Webb, D. F., & Howard, R. A. (1994). The solar cycle variation of coronal mass ejections  
930 and the solar wind mass flux. *Journal of Geophysical Research: Space Physics*, *99*(A3),  
931 4201–4220. doi: <https://doi.org/10.1029/93JA02742>
- 932 Weigel, R. (2010). Solar wind density influence on geomagnetic storm intensity. *Jour-*  
933 *nal of Geophysical Research: Space Physics*, *115*(A9). doi: <https://doi.org/10.1029/>  
934 [2009JA015062](https://doi.org/10.1029/2009JA015062)
- 935 Weimer, D. (2001). Maps of ionospheric field-aligned currents as a function of the in-  
936 terplanetary magnetic field derived from dynamics explorer 2 data. *Journal of Geo-*  
937 *physical Research: Space Physics*, *106*(A7), 12889–12902. doi: <https://doi.org/10.1029/>  
938 [2000JA000295](https://doi.org/10.1029/2000JA000295)
- 939 Workayehu, A., Vanhamäki, H., & Aikio, A. (2020). Seasonal effect on hemispheric asymme-  
940 try in ionospheric horizontal and field-aligned currents. *Journal of Geophysical Research:*  
941 *Space Physics*, *125*(10), e2020JA028051. doi: <https://doi.org/10.1029/2020JA028051>
- 942 Yokoyama, N., & Kamide, Y. (1997). Statistical nature of geomagnetic storms. *Journal*  
943 *of Geophysical Research: Space Physics*, *102*(A7), 14215–14222. doi: <https://doi.org/>  
944 [10.1029/97JA00903](https://doi.org/10.1029/97JA00903)
- 945 Zhang, Y., Sun, W., Feng, X., Deehr, C., Fry, C., & Dryer, M. (2008). Statistical anal-  
946 ysis of corotating interaction regions and their geoeffectiveness during solar cycle 23.  
947 *Journal of Geophysical Research: Space Physics*, *113*(A8). doi: <https://doi.org/10.1029/>  
948 [2008JA013095](https://doi.org/10.1029/2008JA013095)
- 949 Zhao, H., & Zong, Q.-G. (2012). Seasonal and diurnal variation of geomagnetic activity:  
950 Russell-mcpherron effect during different imf polarity and/or extreme solar wind condi-  
951 tions. *Journal of Geophysical Research: Space Physics*, *117*(A11). doi: <https://doi.org/>  
952 [10.1029/2012JA017845](https://doi.org/10.1029/2012JA017845)